

Tidal Tails of Minor Mergers II: Comparing Star Formation in the Tidal Tails of NGC 2782¹

Karen A. Knierman

School of Earth & Space Exploration, Arizona State University, 550 E. Tyler Mall, Room PSF-686 (P.O. Box 871404), TEMPE, AZ 85287-1404

karen.knierman@asu.edu

Paul Scowen

School of Earth & Space Exploration, Arizona State University, 550 E. Tyler Mall, Room PSF-686 (P.O. Box 871404), TEMPE, AZ 85287-1404

paul.scowen@asu.edu

Todd Veach

School of Earth & Space Exploration, Arizona State University, 550 E. Tyler Mall, Room PSF-686 (P.O. Box 871404), TEMPE, AZ 85287-1404

tveach@asu.edu

Christopher Groppi

School of Earth & Space Exploration, Arizona State University, 550 E. Tyler Mall, Room PSF-686 (P.O. Box 871404), TEMPE, AZ 85287-1404

cgroppi@asu.edu

Brendan Mullan

Department of Astronomy & Astrophysics, Penn State University, 525 Davey Lab, University Park, PA

mullan@astro.psu.edu

Iraklis Konstantopoulos

Australian Astronomical Observatory, P.O. Box 915, North Ryde NSW 1670

¹Herschel is an ESA space observatory with science instruments provided by European-led Principal Investigator consortia and with important participation from NASA.

iraklis@aao.gov.au

Patricia M. Knezek

WIYN Consortium, Inc., 950 N. Cherry Avenue, Tucson, AZ 85719

pknezek@noao.edu

Jane Charlton

*Department of Astronomy & Astrophysics, Penn State University, 525 Davey Lab,
University Park, PA*

ABSTRACT

The peculiar spiral NGC 2782 is the result of a minor merger with a mass ratio $\sim 4 : 1$ occurring ~ 200 Myr ago. This merger produced a molecular and HI rich, optically bright Eastern tail and an HI-rich, optically faint Western tail. Non-detection of CO in the Western Tail by Braine et al. (2001) suggested that star formation had not yet begun. However, deep *UBVR* and $H\alpha$ narrowband images show evidence of recent star formation in the Western tail, though it lacks massive star clusters and cluster complexes. Using Herschel PACS spectroscopy, we discover $158\mu\text{m}$ [CII] emission at the location of the three most luminous $H\alpha$ sources in the Eastern tail, but not at the location of the even brighter $H\alpha$ source in the Western tail. The Western tail is found to have a normal star formation efficiency (SFE), but the Eastern tail has a low SFE. The lack of CO and [CII] emission suggests the Western tail HII region may have a low carbon abundance and be undergoing its first star formation. The Western tail is more efficient at forming stars, but lacks massive clusters. We propose that the low SFE in the Eastern tail may be due to its formation as a splash region where gas heating is important even though it has sufficient molecular and neutral gas to make massive star clusters. The Western tail, which has lower gas surface density and does not form high mass star clusters, is a tidally formed region where gravitational compression likely enhances star formation.

Subject headings: galaxies: interactions — galaxies: individual (NGC 2782) — galaxies: star formation — galaxies: star clusters

1. Introduction

Major mergers (e.g., two equal mass spiral galaxies) can form in their debris ranging from large tidal dwarf galaxies (TDGs) down to star clusters (e.g., Duc, Bournaud, & Masset 2004; Weilbacher et al. 2002; Knierman et al. 2003; Mullan et al. 2011). However, the spectacular displays of major mergers (e.g., NGC 4038/9 “The Antennae”; Whitmore et al. 1999) are relatively rare compared to minor mergers (in this work, defined to be between a dwarf galaxy and spiral galaxy with a mass ratio of < 0.3). This work aims to understand how minor mergers shape galactic structure and also to examine star formation in gas that may be marginally stable.

Observations of young star clusters in tidal debris show varied results, with some tails forming many star clusters, while others only have a few star clusters scattered along the tail or only hosted in the tidal dwarf galaxy. Studies have shown a large amount of neutral hydrogen in tidal debris (Smith 1994; Hibbard et al 1994; Maybhate et al. 2006), but only certain regions with higher gas densities host molecular gas (Smith et al. 1999; Braine et al. 2001). Previous results (Boquien et al. 2011; Knierman et al. 2012) have also shown that star formation in tidal debris does not follow the Kennicutt-Schmidt law. This work aims to compare star formation and gas properties on local and global scales using multiwavelength observations of two tidal tails with different properties in the same system.

The peculiar spiral, NGC 2782, is at a distance of 39.5¹ Mpc (Mould et al. 2000). in the RC3, it is classified as SABa(rs) pec since it has a disturbed center with bright arcs. A starburst is occurring in the central regions (Devereux 1989). NGC 2782 has two tidal tails: an HI-rich, optically faint Western tail extending 5' to the northwest and an Eastern tail which has a concentration of HI and CO at its base, but a gas-poor optically bright knot 2.7' from the center (see Smith 1994). A tidal dwarf galaxy candidate (TDGC) was discovered by Yoshida et al. (1994) in the Eastern tail near the main body of the galaxy. Their optical spectrum confirms its association with NGC 2782 and indicates that it may be metal poor, similar to other TDGs (Duc, Bournaud, & Masset 2004). CO is not detected at the location of massive HI clumps in the Western tail which led Braine et al. (2001) to suggest that the HI in the Western tail of NGC 2782 is not gravitationally bound and “has presumably not had time to condense into H₂ and for star formation to begin.”

To determine the merger age and geometry, Smith (1994) constructed a restricted 3-body dynamical model of NGC 2782. This model reproduces the morphology and HI velocities

¹From NED, corrected for Virgo, Great Attractor, and Shapley, which we will use for the duration of this paper.

which indicates that NGC 2782 may be the result of a merger between a large disk galaxy and a lower mass disk galaxy with a mass ratio of ~ 0.25 occurring ~ 200 Myr ago. However, this model does not include gas dynamics or self-gravity of the particles which could change the results. Further simulations have not been done to test this merger scenario. Merger age can also be inferred by using the maximum tail length (50 kpc) and the disk rotation speed (150 km s^{-1} ; Smith (1994)) (see Section 3.1 of Knierman et al. (2003)). For NGC 2782, we infer a merger age of $50 \text{ kpc}/150 \text{ km s}^{-1} = 300 \text{ Myr}$ which is close to the age from Smith (1994).

Wehner (2005) also studied the tidal debris of NGC 2782 with deep, wide-field imaging and found that the debris in the Eastern and Western plumes has colors both consistent with each other and bluer than the main disk of NGC 2782, suggesting that perhaps the two tails formed from the same dwarf companion that passed through or along the disk of NGC 2782 and was destroyed in the process. However, by examining the m_{HI}/L_B ratios for the stellar and gaseous debris, Wehner (2005) concludes that it is unlikely that all the gaseous debris in the Western plume originated in the smaller companion, as this would require the excessively large m_{HI}/L_B ratio of 6.4. More likely, a significant amount of the gaseous debris originated in the gaseous disk of the main galaxy.

NGC 2782 also has a well-behaved exponential disk at intermediate radii. Smith et al. (1994) find an $R^{1/4}$ profile within the innermost arcminute, and Wehner (2005) finds that the $R^{1/4}$ profile reemerges at higher radii, consistent with the idea that the outer stellar plumes are debris resulting from a minor merger. Mullan et al. (2011) in their V and I band *Hubble Space Telescope*/WFPC2 survey of tidal tails find 87 star cluster candidates in the Eastern tail of NGC 2782 and 10 candidates in the Western tail.

We obtained deep optical broadband and $\text{H}\alpha$ images combined with new [CII] and CO observations and published HI and CO observations to compare local and global star formation, as determined by several different tracers, between the tidal tails in NGC 2782. Section 2 contains the observations and calibrations. Section 3 presents the results. In Section 4, we discuss the possible reasons for the differences between the tidal tails.

2. Observations and Reductions

We examine different tracers of star formation in the tidal tails of NGC 2782. First, we examine both tails for evidence of young star clusters using ground-based $UBVR$ images and HST/WFPC2 images to identify isolated star clusters or star cluster complexes. The HST/WFPC2 images are from the Cycle 16 program 11134 (P.I. K. Knierman) and published

in Mullan et al. (2011). Next, we identify young star forming regions using $H\alpha$ and $[CII]$. Then we examine the amount of gas available for star formation through new and published CO observations and previous HI observations.

2.1. Optical images

Images in $UBVR$ and $H\alpha$ were taken with the Loral 2K CCD imager at the Lennon 1.8m *Vatican Advanced Technology Telescope (VATT)* on Mount Graham, Arizona (see Table 1 for a log of observations and Figures 1 and 2). This imager has a $6.4'$ field of view with $0.42''$ per pixel. Images were reduced using standard IRAF² tasks.

2.1.1. Source Detection and Photometry

To select sources, IRAF-DAOFIND was used with a threshold of 4σ where σ is the standard deviation of the background. The standard deviation of the background was found by averaging several regions around the image, away from the varying background of the tail. Sources with $S/N > 3.0$ were retained for photometry due to the smoothness of the ground-based imaging.

Aperture photometry was performed on these sources using the PHOT task in the IRAF-APPHOT package. The radii of the object aperture, the inner boundary of the background annulus, and the outer boundary were 8, 13, and 18 pixels, respectively (3.4/5.5/7.6 arcsec). We retained only sources that were detected in all bands ($UBVR$) and with magnitude errors < 0.2 . Photometric zero-points were obtained using Landolt standard stars taken on photometric nights. The foreground extinction from the Galaxy was corrected using the A_B values from Schlegel, Finkbeiner, & Davis (1998) and the reddening curve from Mathis (1990).

2.1.2. Selection of In Tail and Out of Tail Regions

To obtain a population of background objects we identified “in tail” and “out of tail” regions. Previous studies have used various techniques to determine tail boundaries, including

²IRAF is distributed by the National Optical Astronomy Observatory, which is operated by the Association of Universities for Research in Astronomy, Inc., under cooperative agreement with the National Science Foundation.

Table 1. Optical Observations of NGC 2782

Tail	Date	Filter	Exp. Time sec	Photometric?
Eastern Tail	Feb. 15, 2004	U	12×300	yes
	Feb. 17, 2004	U	3×900	no
	Feb. 15, 2004	B	9×300	yes
	Feb. 17, 2004	V	4×900	no
	May 12, 2005	V	2×300	yes
	Feb. 17, 2004	R	3×900	no
	May 12, 2005	R	2×300	yes
	May 12, 2005	H α	3×1200	yes
	Western Tail	Feb. 18, 2004	U	8×900
May 22, 2004		U	2×600	yes
Feb. 16, 2004		B	4×900	no
May 22, 2004		B	2×300	yes
Feb. 17, 2004		V	4×900	no
May 22, 2004		V	2×300	yes
Feb. 17, 2004		R	3×900	no
May 22, 2004		R	2×300	yes
Oct. 3, 2004		R	3×150	yes
Oct. 4, 2004		R	2×300	yes
Oct. 3, 2004		H α	3×900	yes
Oct. 4, 2004		H α	2×1200	yes
Dec. 6, 2004		H α	3×900	no

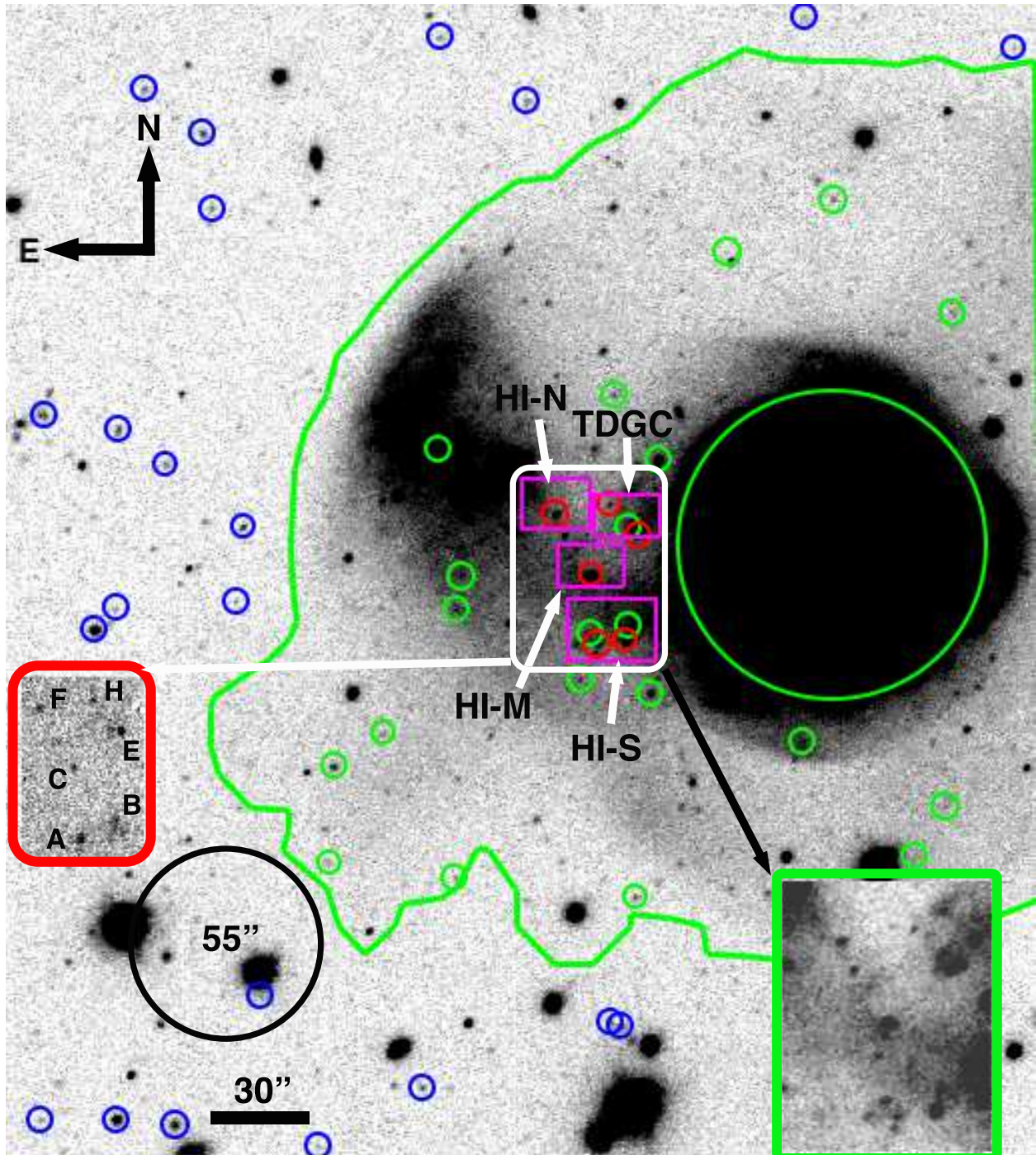


Fig. 1.— V image of Eastern tail taken at the *VATT* 1.8m with final star cluster candidates marked by small circles. Green indicates “in tail”, while Blue indicates “out of tail”. The large green circle indicates the area defined as the central region of the galaxy. Red circles mark the locations of $H\alpha$ sources. Magenta boxes mark the locations of massive HI clouds (Smith 1994). The inset outlined in red shows the $H\alpha$ emission from the area indicated by the white box. The inset image outlined in green shows an enlargement of the region of the V image indicated by the white box. The black circle indicates the beam size of the CO(1-0) observations with the ARO Kitt Peak 12 meter telescope.

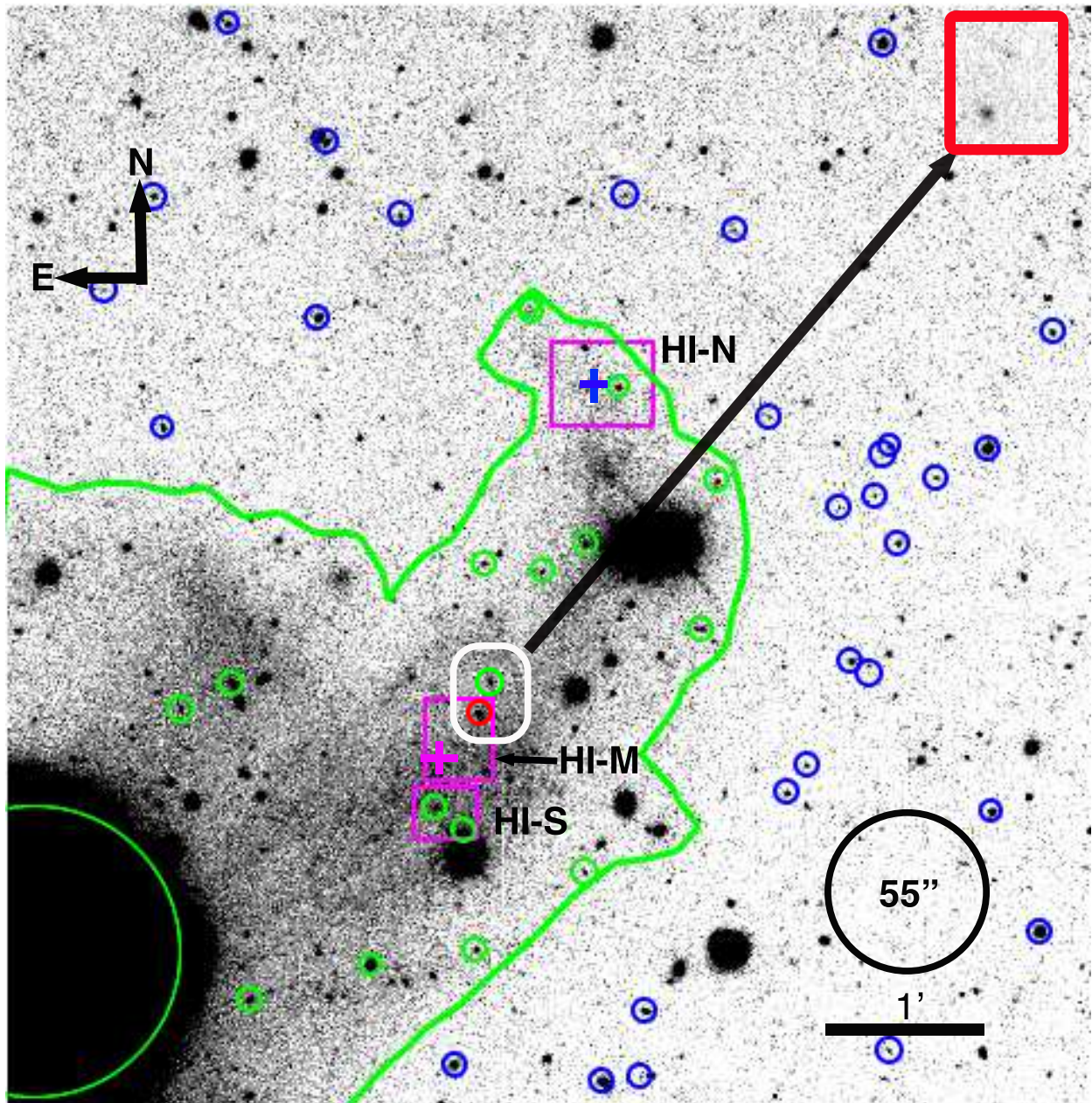


Fig. 2.— V image of Western tail taken at the *VATT* 1.8m with final star cluster candidates marked by small circles. Green indicates “in tail”, while Blue indicates “out of tail”. The large green circle indicates the area defined as the central region of the galaxy. Red circles mark the location of the $H\alpha$ source, W235 (Knierman et al. 2012). Magenta boxes mark the locations of massive H I clouds (Smith 1994). The crosses denote the locations where Smith et al. (1999) looked for CO. The blue cross was reobserved with more sensitive observations by Braine et al. (2001). The inset shows the $H\alpha$ emission from the area indicated by the white box. The black circle indicates the beam size of the CO(1-0) observations with the ARO Kitt Peak 12 meter telescope.

location of the HI contours (Knierman et al. 2003), surface brightness contours at a specific surface brightness (μ) (Schombert, Wallin, & Struck–Marcell 1990), and visual inspection (Bastian et al. 2005b). For this study, a combination of surface brightness and contour plotting methods was used. There are two areas to define for tidal debris: the inner regions of the galaxy must be excluded to prevent contamination from star clusters formed in the dense inner starburst, and the outer extent of the debris region where the debris fades into the general sky background.

To determine where the disk of the galaxy ends and the debris begins, we considered the use of the standard D_{25} system or the isophotal diameter at the limiting surface brightness of 25 B mag arcsec⁻². The major and minor axes and the position angle of the D_{25} parameters were taken from LEDA³, and assuming an ellipse, plotted on the image. Next, logarithmically spaced surface brightness contours were plotted on the image to determine where the regularity of the central galaxy region departed into the asymmetry of the debris region. The boundary between the central region of the galaxy and the tidal debris was then defined to be a combination of the D_{25} ellipse and the last regularly shaped contour.

To determine the divide between the debris region and the general background, again, a combination of contour plots and surface brightness limits was used. We first plot the Holmberg radius (Holmberg 1958), the radius at which the surface brightness in a blue filter reaches 26.5 mag arcsec⁻². This contour at $\mu_B = 26.5$ mag arcsec⁻², followed not the central regions of this galaxy, but the outer boundary of the tidal tails and debris regions. Holmberg found that the radius at which $\mu_B = 26.5$ mag arcsec⁻² included the outermost HII or star forming regions in a galaxy, however, recent work shows this to not always be the case (Elmegreen & Hunter 2004). It is, therefore, not surprising that the Holmberg radius in this merger includes the tidal debris with its star formation. To ensure inclusion of all tidal debris, we plot logarithmically spaced surface brightness contours on the images. At the edges of the tidal debris, there was a rapid decline in surface brightness denoted by the small spacing of several contours followed by 2 surface brightness contours with larger spacing before the tidal debris faded into the background. The outermost contour that enclosed the tail region was chosen to represent the tidal tail. Upon inspection, this contour followed approximately the Holmberg contour, however, where they differed greatly, the contour chosen by contour spacing was preferred. Figures 1 and 2 indicate the tidal tail regions selected.

³HyperLeda database (<http://leda.univ-lyon1.fr>) Paturel et al. (2003)

2.1.3. Completeness Tests

Completeness tests were conducted on the images in each band. First, a PSF was constructed using 6-10 bright, isolated stars in each image with the PSF task. Then ADDSTAR was used to add 100 stars randomly distributed across the image. Stars were added in 0.5 mag bins spanning the range from 13-26.5 instrumental magnitudes (e.g., an image with 100 stars added with magnitudes between 13 and 13.5, a second image with 100 stars added with magnitudes between 13.5 and 14). Sources were detected and photometry performed as described in Section 2.1.1. This procedure was run 50 times per image to produce a total of 5000 stars added randomly to each image. As seen in Figure 3, the completeness limit for the Eastern Tail is $V \sim 22.9$ ($M_V \sim -10.1$) and for the Western Tail is $V \sim 23.7$ ($M_V \sim -9.3$). The higher background of the Eastern tail may account for the completeness limit at a brighter magnitude.

2.1.4. Final Star Cluster Candidates

To select the final sample of star cluster candidates, we used the 3DEF method (Bik et al. 2003), a three dimensional maximum likelihood code which fits the spectral energy distribution (SED) of a cluster to broad band colors, to fit cluster ages, masses, and extinctions (number of data points = 4, parameters in model = 3). For each cluster, the 3DEF method uses a grid of simple stellar population (SSP) models of ages between 1 Myr and 10 Gyr, extinctions ranging from $0 \leq A_V \leq 4$ in equal steps of 0.02, and masses with a range depending on the absolute magnitude of the source. For this analysis, we adopt the models of Bruzual & Charlot (2003) with a metallicity of $0.4Z_\odot$. We assume that the metallicity of the star clusters in the tidal debris matches the observed metallicity of tidal dwarf galaxies, $Z \sim 1/3Z_\odot$ (Duc, Bournaud, & Masset 2004), which is similar to the metallicity of the outer regions of spiral galaxies. Table 2 lists the information for star cluster candidates in the Eastern tail. Tables 3 and 4 list the information for star cluster candidates in the Western tail. Table 3 shows properties of the star clusters such as reduced χ^2 , extinction, age, and mass, and their associated errors as well as the centroid pixel values. Table 2 and 4 show star cluster photometry and errors in $UBVR$, colors, and M_B .

The errors in the magnitudes in each band were used to estimate the errors in the age, mass, and extinction. For each $UBVR$ magnitude, we add the error in the magnitude to the magnitude and run the SED fitting code - the output ages, masses, and extinctions are the upper bound on the error bar for those values. Then we subtract the error in the magnitude from each $UBVR$ magnitude and run the SED fitting code - the output ages, masses, and ext. are the lower bound on the error bar for those values. For bright sources with small

error bars, if the output age, mass, or extinction were the same as the data values, the upper and/or lower bounds for the errors were taken from the grid size of the models. For example, a SCC may have an output age of 6.42 with the same age given when we run both “error” models. The next highest age bin is 6.44, so this is assigned to be the upper error and the next lowest age bin, 6.40, will be the lower error. (See the star cluster candidates with their errors in age, mass, and extinction in Table 3.)

For the whole Eastern tail image field, out of 153 sources selected in the above method, a total of 55 had reduced $\chi^2 < 3.0$ when fit to the Bruzual & Charlot (2003) single stellar population models with 29 residing in the tail region. For the Western tail image field, out of 113 sources selected in the above method, a total of 49 had reduced $\chi^2 < 3.0$ with 18 in the tail region.

In the “out of tail” regions, 18 were fit in the Eastern tail image and 30 in the Western tail image. These represent our contaminants. Very red sources fit with large extinction are likely to be foreground stars that have similar colors. Others may be background galaxies. To estimate the number of foreground stars in our images, we use the Besaon Milky Way star count model by Robin et al. (2003). For location of NGC 2782 in the sky, the 6’ field of view, and the range of colors and apparent magnitudes of our SCCs, we estimate there to be about 13 foreground stars. Since the Eastern tail contains about 40% of the field of view, we then expect about 5 foreground stars within the tail and 8 in the “out of tail” region. The Western tail occupies about 30% of the field of view, so we expect about 4 foreground stars in the “in tail” region and 9 in the “out of tail” region. Using the Sloan Digital Sky Survey SkyServer DR6 Search (Adelman-McCarthy et al. 2008) and the Jester et al. (2005) transformations from $UBVR$ to ugr filters, our range of color and magnitudes for the sources in the Eastern and Western tail estimate about 11 background galaxies in the Eastern tail entire field of view and about 18 in the Western tail field of view. The transformation from $UBVR$ to ugr filters is uncertain, so these numbers are only rough estimates for the background galaxies based on color and brightness. In total, we estimate about 19 foreground stars and background galaxies for the Eastern tail (close to the 18 found in the “out of tail” region) and 27 in the Western tail (close to the 30 found “out of tail”). The locations of the final star cluster candidates and the “out of tail” sources fit by the SSP models are marked on the V images in Figures 1 and 2.

Table 2. NGC 2782 East Star Cluster Candidate Photometry

#	X	Y	U	B	V	R	U - B	B - V	V - R	M_B
0	394.152	565.963	21.855 (0.069)	22.343 (0.097)	21.550 (0.087)	21.027 (0.103)	-0.488 (0.119)	0.793 (0.130)	0.522 (0.135)	-10.647
1	360.460	474.580	21.123 (0.039)	20.998 (0.035)	20.772 (0.038)	20.394 (0.070)	0.125 (0.052)	0.226 (0.051)	0.377 (0.080)	-11.992
2	398.524	507.196	21.269 (0.029)	21.282 (0.028)	21.109 (0.055)	20.521 (0.064)	-0.013 (0.041)	0.172 (0.062)	0.588 (0.084)	-11.708
3	429.452	456.452	22.053 (0.058)	22.250 (0.068)	21.736 (0.096)	22.012 (0.265)	-0.197 (0.090)	0.514 (0.118)	-0.276 (0.281)	-10.740
4	383.717	448.772	22.285 (0.085)	22.292 (0.092)	23.056 (0.305)	22.089 (0.303)	-0.007 (0.125)	-0.764 (0.319)	0.967 (0.430)	-10.698
61	196.373	192.751	23.320 (0.195)	22.979 (0.115)	22.529 (0.108)	21.918 (0.116)	0.341 (0.226)	0.450 (0.158)	0.611 (0.159)	-10.011
72	285.484	236.534	23.175 (0.147)	23.057 (0.072)	22.724 (0.118)	21.894 (0.122)	0.118 (0.164)	0.333 (0.138)	0.830 (0.169)	-9.933
86	95.453	288.121	23.745 (0.231)	23.937 (0.163)	22.978 (0.148)	21.661 (0.100)	-0.192 (0.282)	0.959 (0.220)	1.317 (0.179)	-9.053
146	380.222	357.056	23.619 (0.176)	23.474 (0.132)	22.652 (0.132)	22.100 (0.176)	0.146 (0.220)	0.822 (0.187)	0.552 (0.220)	-9.516
233	527.075	402.355	22.547 (0.091)	22.002 (0.057)	21.018 (0.063)	20.286 (0.056)	0.544 (0.108)	0.984 (0.085)	0.732 (0.084)	-10.988
248	343.433	410.918	20.778 (0.022)	20.426 (0.015)	19.831 (0.017)	19.445 (0.025)	0.352 (0.027)	0.595 (0.023)	0.386 (0.031)	-12.564
358	367.965	467.203	21.705 (0.081)	21.590 (0.067)	20.858 (0.048)	20.410 (0.079)	0.115 (0.104)	0.732 (0.082)	0.448 (0.092)	-11.400
451	508.510	508.326	23.259 (0.145)	23.299 (0.117)	22.577 (0.163)	21.743 (0.184)	-0.041 (0.186)	0.723 (0.201)	0.834 (0.246)	-9.691
506	512.762	536.482	23.581 (0.214)	23.424 (0.175)	22.092 (0.144)	21.492 (0.162)	0.158 (0.277)	1.332 (0.226)	0.600 (0.217)	-9.566
530	367.374	549.503	21.755 (0.044)	22.137 (0.059)	21.887 (0.125)	21.191 (0.136)	-0.382 (0.073)	0.250 (0.138)	0.696 (0.185)	-10.853
543	399.654	556.366	22.271 (0.091)	22.348 (0.076)	22.048 (0.129)	21.258 (0.126)	-0.077 (0.119)	0.300 (0.149)	0.790 (0.180)	-10.642
555	370.081	562.678	20.858 (0.028)	20.996 (0.033)	20.579 (0.045)	20.358 (0.080)	-0.138 (0.043)	0.417 (0.056)	0.222 (0.092)	-11.994
596	408.717	595.590	24.289 (0.389)	23.949 (0.184)	22.993 (0.187)	21.622 (0.166)	0.341 (0.430)	0.955 (0.262)	1.371 (0.250)	-9.041
611	349.476	607.032	22.658 (0.078)	22.272 (0.054)	21.382 (0.055)	20.347 (0.054)	0.386 (0.095)	0.891 (0.077)	1.034 (0.077)	-10.718
640	573.743	640.455	23.826 (0.218)	23.435 (0.105)	22.894 (0.133)	22.026 (0.137)	0.392 (0.242)	0.541 (0.170)	0.868 (0.191)	-9.555
650	221.230	646.889	23.340 (0.177)	22.784 (0.094)	21.943 (0.113)	21.266 (0.146)	0.556 (0.201)	0.842 (0.147)	0.676 (0.185)	-10.206
655	614.905	668.400	23.104 (0.122)	22.772 (0.054)	21.566 (0.047)	20.696 (0.040)	0.332 (0.133)	1.206 (0.071)	0.870 (0.061)	-10.218
665	101.749	702.029	23.494 (0.158)	23.433 (0.121)	22.704 (0.123)	21.983 (0.149)	0.061 (0.199)	0.729 (0.172)	0.721 (0.193)	-9.557
682	127.326	743.661	24.429 (0.472)	23.557 (0.159)	22.433 (0.121)	21.004 (0.071)	0.872 (0.498)	1.124 (0.200)	1.428 (0.140)	-9.433
684	619.316	749.198	23.525 (0.184)	23.915 (0.150)	22.963 (0.172)	22.324 (0.169)	-0.390 (0.238)	0.952 (0.228)	0.639 (0.241)	-9.075
690	513.713	761.758	24.085 (0.285)	23.810 (0.154)	22.902 (0.128)	22.095 (0.126)	0.275 (0.324)	0.907 (0.200)	0.807 (0.179)	-9.180
695	362.009	777.885	22.894 (0.099)	22.835 (0.059)	22.276 (0.075)	22.125 (0.125)	0.060 (0.115)	0.558 (0.095)	0.151 (0.145)	-10.155

Table 3. NGC 2782 West Star Cluster Candidate Properties

Number	χ^2	Extinction $E(B - V)$	Age $\log(\text{yr})$	Mass $\log(M/M_\odot)$	X	Y
					pixel	
97	0.1	$0.50^{0.49}_{0.51}$	$7.58^{7.54}_{7.63}$	$5.67^{5.68}_{5.66}$	501.704	266.439
101	0.6	$0.27^{0.26}_{0.21}$	$8.06^{8.01}_{8.21}$	$5.73^{5.75}_{5.70}$	498.146	270.219
120	0.0	$0.63^{0.61}_{0.64}$	$7.76^{7.70}_{7.81}$	$6.15^{6.10}_{6.16}$	421.899	338.391
152	2.5	$0.97^{0.96}_{0.98}$	$6.40^{6.38}_{6.42}$	$5.96^{5.97}_{5.95}$	334.414	421.170
172	1.3	$0.00^{0.00}_{0.01}$	$8.46^{8.51}_{8.40}$	$5.74^{5.82}_{5.70}$	451.681	477.299
182	0.2	$0.99^{0.98}_{1.01}$	$6.44^{6.40}_{6.46}$	$5.75^{5.82}_{5.74}$	541.170	494.540
185	0.7	$1.21^{1.18}_{1.25}$	$6.34^{6.32}_{6.36}$	$6.06^{6.07}_{6.05}$	489.818	501.482
204	0.0	$1.42^{1.38}_{1.46}$	$6.34^{6.36}_{6.26}$	$6.57^{6.55}_{6.65}$	348.104	552.657
226	0.5	$0.01^{0.03}_{0.00}$	$7.53^{7.49}_{7.54}$	$5.05^{5.07}_{5.01}$	536.171	599.457
227	0.9	$0.26^{0.82}_{0.28}$	$9.30^{7.86}_{9.32}$	$7.06^{6.70}_{7.08}$	764.120	600.468
234	0.0	$0.94^{0.92}_{0.96}$	$6.40^{6.42}_{6.32}$	$5.66^{5.67}_{5.76}$	810.621	623.717
235	0.6	$0.57^{0.58}_{0.64}$	$6.58^{6.60}_{6.22}$	$5.35^{5.39}_{5.80}$	545.504	626.576
282	0.0	$0.17^{0.20}_{0.15}$	$7.86^{7.76}_{7.91}$	$5.30^{5.34}_{5.25}$	584.557	710.380
299	0.1	$0.78^{0.77}_{0.75}$	$7.91^{7.81}_{8.11}$	$6.56^{6.52}_{6.60}$	558.372	730.295
331	1.2	$0.82^{0.81}_{0.83}$	$6.40^{6.44}_{6.38}$	$5.48^{5.46}_{5.45}$	452.459	767.836
398	2.4	$0.57^{0.55}_{0.52}$	$7.86^{7.72}_{8.11}$	$5.94^{5.88}_{5.97}$	548.341	836.734
412	0.2	$1.21^{1.22}_{1.20}$	$7.32^{7.26}_{7.42}$	$6.98^{6.95}_{7.01}$	641.640	850.058
448	0.6	$0.75^{0.71}_{0.81}$	$6.82^{6.84}_{6.80}$	$5.39^{5.37}_{5.41}$	749.070	880.521

Table 4. NGC 2782 West Star Cluster Candidate Photometry

#	U	B	V	R	$U - B$	$B - V$	$V - R$	M_B
97	23.274 (0.134)	23.411 (0.099)	22.814 (0.092)	22.290 (0.079)	-0.136 (0.166)	0.596 (0.135)	0.524 (0.121)	-9.579
101	22.967 (0.102)	23.061 (0.074)	22.610 (0.081)	22.327 (0.078)	-0.094 (0.126)	0.451 (0.109)	0.283 (0.112)	-9.929
120	23.076 (0.111)	23.016 (0.065)	22.330 (0.072)	21.690 (0.051)	0.060 (0.129)	0.686 (0.097)	0.640 (0.088)	-9.974
152	22.503 (0.080)	22.978 (0.065)	22.375 (0.067)	21.569 (0.046)	-0.475 (0.103)	0.603 (0.093)	0.806 (0.081)	-10.012
172	22.635 (0.085)	22.573 (0.061)	22.369 (0.104)	22.307 (0.140)	0.062 (0.105)	0.204 (0.120)	0.063 (0.174)	-10.417
182	23.058 (0.120)	23.488 (0.108)	22.739 (0.098)	22.066 (0.075)	-0.430 (0.161)	0.749 (0.145)	0.673 (0.123)	-9.502
185	23.621 (0.168)	23.832 (0.153)	23.045 (0.120)	22.063 (0.082)	-0.211 (0.227)	0.787 (0.195)	0.983 (0.145)	-9.158
204	23.398 (0.155)	23.429 (0.100)	22.347 (0.082)	21.309 (0.039)	-0.031 (0.184)	1.082 (0.129)	1.037 (0.091)	-9.561
226	22.376 (0.063)	22.841 (0.062)	22.883 (0.113)	22.599 (0.108)	-0.465 (0.088)	-0.042 (0.129)	0.283 (0.156)	-10.149
227	22.917 (0.134)	22.637 (0.042)	21.658 (0.040)	20.944 (0.025)	0.281 (0.140)	0.979 (0.058)	0.714 (0.047)	-10.353
234	23.163 (0.175)	23.585 (0.108)	22.918 (0.135)	22.297 (0.095)	-0.422 (0.206)	0.666 (0.173)	0.621 (0.165)	-9.405
235	21.903 (0.040)	22.492 (0.047)	22.075 (0.059)	21.741 (0.055)	-0.589 (0.062)	0.417 (0.075)	0.334 (0.080)	-10.498
282	23.171 (0.129)	23.404 (0.102)	23.143 (0.148)	22.888 (0.141)	-0.234 (0.165)	0.261 (0.180)	0.255 (0.204)	-9.586
299	23.064 (0.142)	22.793 (0.075)	21.980 (0.083)	21.192 (0.050)	0.270 (0.161)	0.814 (0.112)	0.788 (0.097)	-10.197
331	22.991 (0.112)	23.660 (0.128)	22.999 (0.113)	22.461 (0.095)	-0.669 (0.170)	0.661 (0.171)	0.538 (0.148)	-9.330
398	23.519 (0.184)	23.348 (0.109)	22.990 (0.136)	22.152 (0.085)	0.171 (0.214)	0.358 (0.174)	0.838 (0.161)	-9.642
412	22.849 (0.099)	22.556 (0.046)	21.377 (0.028)	20.245 (0.015)	0.293 (0.109)	1.179 (0.054)	1.132 (0.032)	-10.434
448	23.296 (0.173)	23.358 (0.088)	22.350 (0.063)	21.599 (0.046)	-0.062 (0.194)	1.008 (0.109)	0.751 (0.078)	-9.632

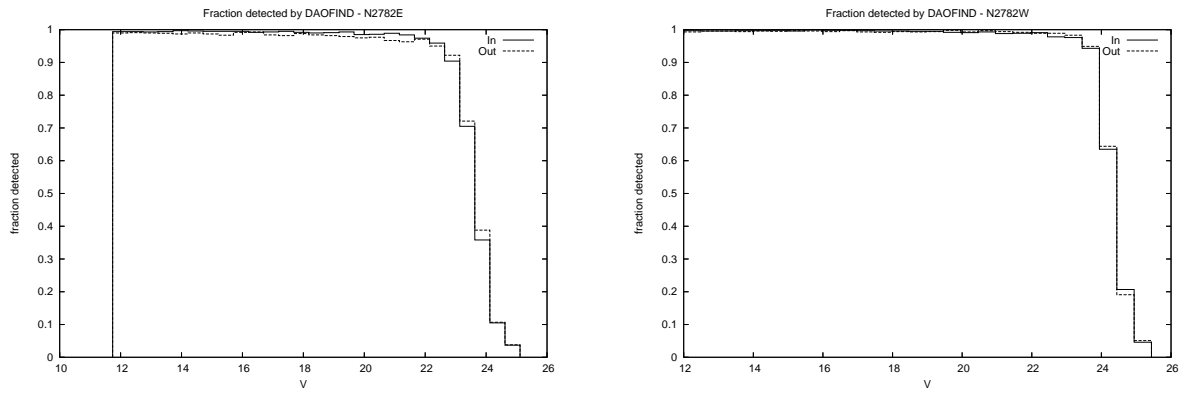


Fig. 3.— For Eastern Tail (left) and Western Tail (right), the fraction of artificial stars recovered by DAOFIND in the V band.

2.2. H α Images

Narrow-band H α images were also obtained at the *VATT* with an 88 mm Andover 3-cavity interference filter centered at 6630 Å. The FWHM of the filter is 70Å which includes the [NII] lines. Integration times for the H α images were 3×1200 s on the Eastern tail and 2×1200 s and 6×900 on the Western tail. To subtract continuum emission, both fields were also observed with a Kron-Cousins *R* filter using integration times of 3×300 s. Images were reduced in a similar manner as stated above.

To create images with only the emission lines, a scaled *R* band image was subtracted from narrowband image after alignment using foreground stars. To determine an initial scaling factor, the ratio of integration time for individual frames is multiplied by the ratio of filter widths. If there were still strong continuum features in the galaxies, the scaling factor was varied iteratively until the continuum-dominated regions in the galaxy and the background source and foreground star residuals reached a minimum (Lee 2006). The insets in Figures 1 and 2 show the continuum-subtracted H α images for the regions of interest.

2.2.1. Calibration of H α

Spectrophotometric standard stars from the Oke (1990) catalog were observed on each night. Aperture photometry of these standards was compared to their absolute magnitudes. Absolute magnitudes for each spectrophotometric standard star were calculated by integrating their spectral energy distribution over the filter response function. As in Lee (2006), we used a standard atmospheric extinction coefficient of $0.08 \text{ mag airmass}^{-1}$. Zeropoints were calculated by comparing the absolute magnitude in each filter with the instrumental magnitude from aperture photometry. For each night, the zeropoints from all standards (typically 3-5) were averaged.

Due to the proximity of the [NII] doublet at $\lambda 6548,6583$ to the H α line, their contribution to the flux needs to be accounted for and removed. Also, the use of the broadband *R* filter for the continuum measurement means that emission line flux from that filter needs to be removed. The total flux equation (Equation A13 in Lee (2006)) is:

$$f_{tot}(\text{H}\alpha + [\text{NII}]) = \lambda^{-2} 10^{-0.4(ZP+2.397-\kappa_{sec}(z))} FWHM_{NB} CR(\text{H}\alpha + [\text{NII}]) \left[T_{NB}(\lambda) - T_R(\lambda) \frac{t_R}{t_{NB}} \frac{1}{F} \right]^{-1} \quad (1)$$

λ : redshifted wavelength of H α

ZP : zero point

κ : atmospheric extinction coefficient (we use $0.08 \text{ mag airmass}^{-1}$)

$FWHM_{NB}$: width of narrowband filter in Å

$CR(H\alpha + [NII])$: count rate in continuum subtracted image

T_R : Transmission correction in R . Calculated by an average of normalized transmissions at each redshifted wavelength of $H\alpha$ and $[NII]$ lines, weighted by their relative line fluxes.

T_{NB} : Transmission correction for narrowband filter. Calculated by an average of normalized transmissions at each redshifted wavelength of $H\alpha$ and $[NII]$ lines, weighted by their relative line fluxes.

t_R : exposure time in R band filter

t_{NB} : exposure time in narrowband filter

F : scale factor applied to R band continuum image when subtracting it from narrowband image.

While T_{NB} would ideally be calculated by measuring the line ratios of $H\alpha$ and $[NII]$ lines directly from spectroscopy, in the absence of spectra for HII regions, there is a relation between metallicity and the ratio of $[NII]$ to $H\alpha$. In Figure 9 of van Zee et al. (1998), an empirical relation is shown between these two values:

$$12 + \log(O/H) = 1.02\log([NII]/H\alpha) + 9.36 \quad (2)$$

For the metallicity of $0.4Z_{\odot}$, as used in the single stellar population models to fit the star cluster candidates, $12 + \log(O/H) = 8.06$ which gives $\log([NII]/H\alpha) = -1.3$. These numbers were also used to subtract the flux of the $[NII]$ lines, giving a resulting flux that contains only that of $H\alpha$. If we instead use the value of $12 + \log(O/H) = 8.72$ as measured by Werk et al. (2011) in the Western tail of NGC 2782, we find $\log([NII]/H\alpha) = -0.63$. Using this value to determine our $H\alpha$ flux, we find that for the Western tail region the difference between the $H\alpha$ luminosity for the higher metallicity ratio and for the lower metallicity ratio is $0.1 \times 10^{38} \text{ erg s}^{-1}$ which is less than the error bar ($\pm 0.4 \times 10^{38} \text{ erg s}^{-1}$). We adopt the lower metallicity value for this work.

2.3. $[CII]$ observations

To map the $[CII]$ $158\mu\text{m}$ fine structure line in the tidal tails of NGC 2782, we used the PACS spectrometer (Poglitsch et al. 2010) on the *Herschel Space Observatory* (Pilbratt et al. 2010). The $[CII]$ $158\mu\text{m}$ line is observed with the 2nd plus 1st order gratings. We used pointed observations with chopping/nodding and a large throw of $6'$ off the source. To increase the line sensitivity, we set the line repetition factor to the maximum value of 10 for each target.

To increase the total sensitivity, we repeat each observation cycle 3 times. To reach the needed depth, we observed each pointing for 3.1 hours.

We observed at one location in each tidal tail corresponding to areas of recent star formation as shown by $H\alpha$ emission indicated in our narrowband images. The PACS array has a total field of view of $47'' \times 47''$ with 5×5 spatial pixels of $9.4''$ size. Each spatial pixel has 16 spectral elements. This size easily encompasses the star forming region in the Western tail of NGC 2782 (Knierman et al. 2012). The Eastern tail of NGC 2782 has a larger spatial extent of star formation; we choose to target only the area with the highest observed CO and HI.

The data were processed using the PACS spectrometer pipeline of the Herschel Interactive Processing Environment (HIPE) Version 7.3.0. The resulting PACS Rebinned Spectral Cube product was exported to a fits cube for further analysis using IDL routines. The [CII] line emission peaks at $159.123 \mu\text{m}$ for the sources in the Eastern tail. After subtracting a linear baseline, we produced an integrated intensity map (Fig. 4) by integrating over the wavelength range from $158.997\text{-}159.249\mu\text{m}$. Contours from $3\text{-}10\sigma$ are plotted with $\sigma = 0.0028 \text{ Jy } \mu\text{m pix}^{-1}$. We determine σ by taking the rms of spectra outside the line area, multiplying by the square root of the number of channels integrated for the map (5 in this case), and the width of one channel, $0.063 \mu\text{m}$. Spectra (as shown in Fig. 5) were extracted from a single spaxel from the PACS Rebinned Spectral Cube at the locations indicated in Fig. 4. After subtracting a linear baseline, the line intensities were summed over the same range as above and multiplied by the bandwidth. Errors in the intensity were calculated from the rms value outside the line area. To correct the amount of flux that falls outside the single spaxel, we use a flux correction of $1/0.5$ at $160 \mu\text{m}$ according to Fig. 7 of the PACS Spectroscopy Performance and Calibration Version 2.4 document (Vandenbussche et al. 2011). This aperture correction assumes that the source is a point source lying at the center of the given spaxel.

2.4. CO(1-0) observations

The Eastern tail and Western tail of NGC 2782 were observed in the CO(1-0) line in March and October 2012 using the Arizona Radio Observatory Kitt Peak 12 meter telescope. We used the ALMA band 3 receiver with 2IFs (both polarizations in USB) using the MAC autocorrelator in 800MHz bandwidth mode with 2048 channels. The total bandpass is 1500 km s^{-1} wide and was centered at 2555 km s^{-1} . We observed in position switch mode with a $10'$ throw in azimuth to the off position. The beam size FWHM is $55''$ at 115 GHz . The system temperature ranged from $270\text{-}360\text{K}$. We observed at the same locations of recent star

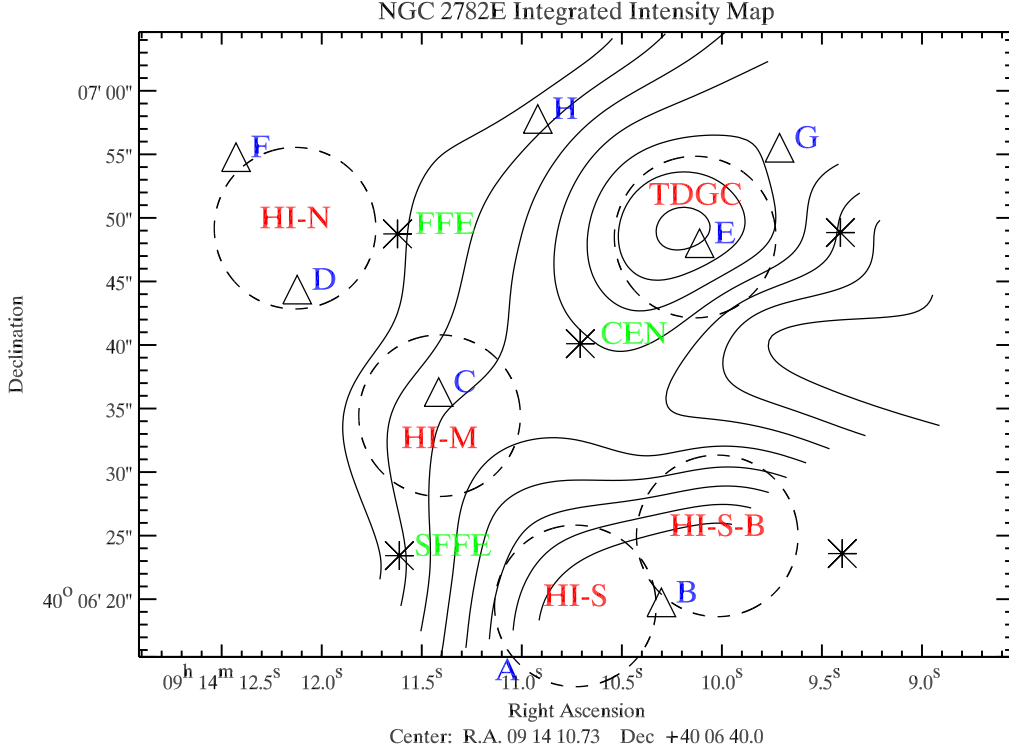


Fig. 4.— Contour of [CII] in Eastern tail of NGC 2782 from Herschel/PACS. Solid contours range from $3 - 10\sigma$ with $\sigma = 0.0028 \text{ Jy } \mu\text{m pix}^{-1}$. Circles with red labels indicate position of extracted spectra shown in Fig. 5. Triangles with blue labels mark the locations of $H\alpha$ sources found here and also listed in Smith et al. (1999). Asterisks mark the locations where CO(1-0) was looked for with the Kitt Peak 12 meter telescope with the green labeled points indicating locations discussed in the text. The location labeled “CEN” was observed in this work (Fig. 6) while all other locations were observed by Smith et al. (1999).

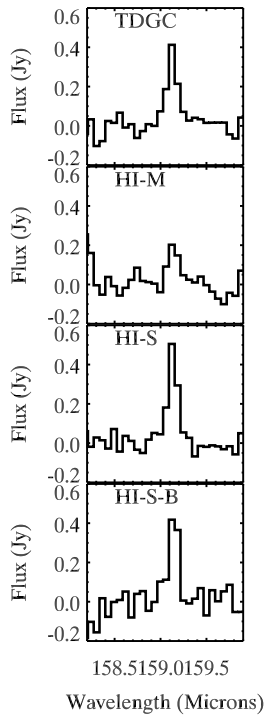


Fig. 5.— Spectra of [CII] extracted at locations in Eastern tail indicated in Fig. 4.

formation in the Eastern and Western tails of NGC 2782 as our [CII] observations. For both tails, we reach an rms value of 1 mK which is deeper than the observations of these tails by Smith et al. (1999). The final summed scan for the Eastern tail location is shown in Fig. 6.

3. Results

As seen in previous work (Smith 1994; Wehner 2005), the deep optical images presented here show that NGC 2782 has an Eastern tail stretching 20 kpc to the northeast. This tail consists of a bright region at the tip with a fainter, yet clumpy bridge region between the main body of the spiral and the bright region at the tip of the tail. There is also a fainter extension to the southeast as well as faint debris to the north and south of the main body of the spiral. The Western tail stretches 50 kpc to the northwest. It has a faint yet clumpy structure along its length. There is a single stream stretching the full 50 kpc as well as a smaller extension to the north which only extends one-third as far.

We now examine several different tracers of star formation between the tidal tails: the young star cluster population, H II regions, and the gas properties including neutral, ionized, and molecular gas.

3.1. Properties of star clusters in the tidal debris of NGC 2782

The final sample of star cluster candidates include 28 sources in the Eastern tail and 19 sources in the Western tail. As seen in Figure 1, the majority (70%) of the star cluster candidates found in the Eastern tail are found in the bridge region. Four candidates are found in the southeast extension while 3 are found in the debris to the north and 3 are found south of the central galaxy. In the Western tail (Fig. 2), the star cluster candidates are mostly located along the main tail with only 2 in the short tail to the north.

3.1.1. *Overdensity of star clusters in the tails*

While it is difficult to remove further contaminants to the star cluster sample without using additional observations (e.g., spectroscopy), an idea of the amount of star clusters in the tidal tails can be determined statistically by subtracting the background density from the “in tail” sample. This technique was used in Knierman et al. (2003) to determine the overdensity of star clusters in the tidal tails of major mergers. In that paper, young star clusters were selected by using $M_V < -8.5$ and $V - I < 0.7$ since only one color was available.

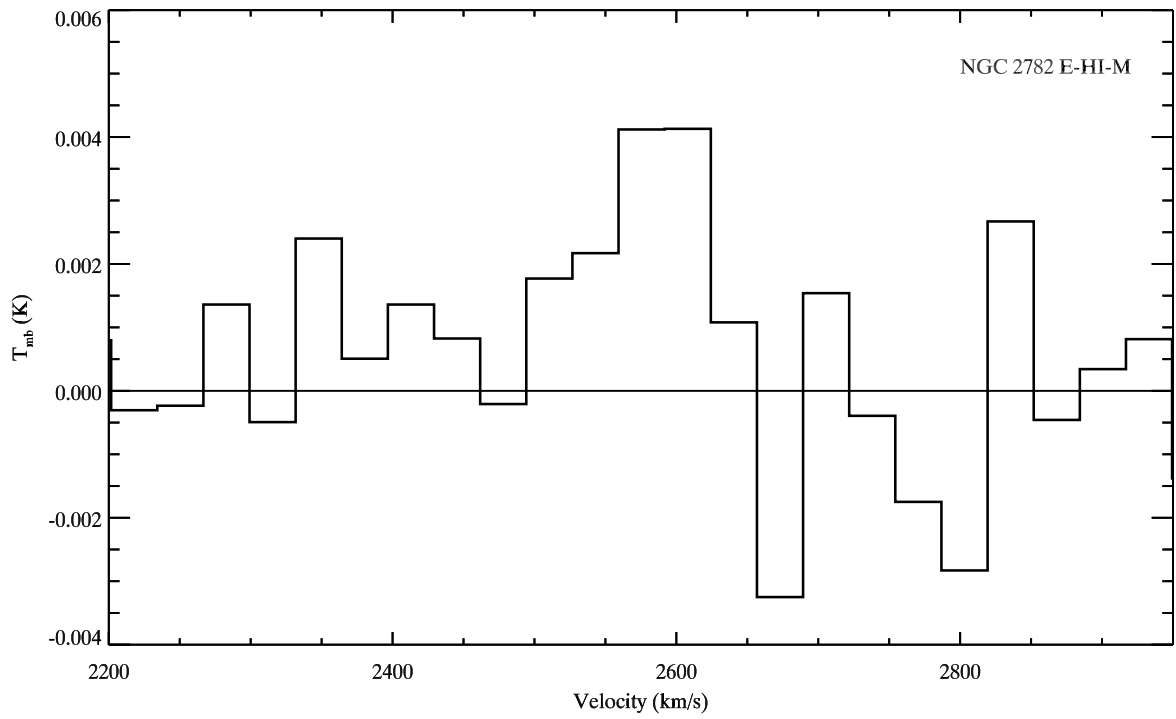


Fig. 6.— Spectra of CO(1-0) in Eastern tail of NGC 2782 from ARO Kitt Peak 12 meter telescope. The location of the observation is the same as the [CII] observation with Herschel.

For this study, we again use $M_V < -8.5$, but since we are unable to match the color cut exactly, we take the Bruzual & Charlot (2003) model age of $\log(\text{age})=8.5$ at which $V-I = 0.7$ as our criteria. Table 5 gives the calculation of the overdensity of young star clusters in the tidal debris. Both the Eastern and Western tails have similar values for the overdensity of 0.005-0.006 star clusters per kpc^2 . This is much lower than the value of 0.108 kpc^{-2} for the Western tail of major merger NGC 3256. Given the differing areas in the Eastern and Western tails, the expected number of actual star clusters is 14 and 10 respectively. In their HST/WFPC2 survey Mullan et al. (2011), also calculate the overdensity of these tails, but for smaller regions within one WFPC2 pointing. Their values are 0.234 and 0.016 kpc^{-2} , respectively. These values are 39 and 3 times larger than the values measured here. We suspect the difference in areas may have a large affect on this calculation so we calculate the overdensity of our star cluster candidates within area of their WFPC2 observation. We find 9 star cluster candidates within this region of the tail, and only 1 that overlaps in the “out of tail” region. This gives an overdensity of 0.02 ± 0.01 for the Eastern tail, now only a factor of ten lower than the value from Mullan et al. (2011).

3.2. Properties of Star Cluster Candidates

As shown in Figure 7, more luminous star cluster candidates are found in the Eastern tail than in the Western tail. The ranges of luminosity are $-12.6 < M_B < -9$ for the Eastern tail and $-10.5 < M_B < -9$ for the Western tail. The average M_B for the Eastern tail is -10.34 , while the average M_B in the Western tail is -9.85 . According to the Kolmogorov-Smirnov test, these distributions of M_B have a probability of $P = 0.019$ of being drawn from the same distribution.

Whitmore et al. (1999) use a faint end cutoff of $M = -9$ since sources fainter than that limit are likely to be bright stars at the distance of the galaxy. The brighter end ($M_B = -12$) corresponds to the luminosity of H II regions in Sa/Sb galaxies (Bresolin & Kennicutt 1997) and to an age of ~ 60 Myr in the Bruzual & Charlot (2003) models for a $10^6 M_\odot$ star cluster. These star cluster candidates are all much more luminous than the Trapezium

Table 5. Overdensity of star clusters in tails

Tail	Pixel size pc	N_{in}	Area $_{in}$ pix 2	Area $_{in}$ kpc 2	N_{in}/kpc^2	N_{out}	Area $_{out}$ pix 2	Area $_{out}$ kpc 2	N_{out}/kpc^2	Surplus
E	80.69	20	345877	2252.0	0.009(0.002)	9	475199	3094.0	0.003(0.001)	0.006(0.002)
W	80.69	17	257238	1674.9	0.010(0.002)	19	584730	3807.2	0.005(0.001)	0.005(0.003)

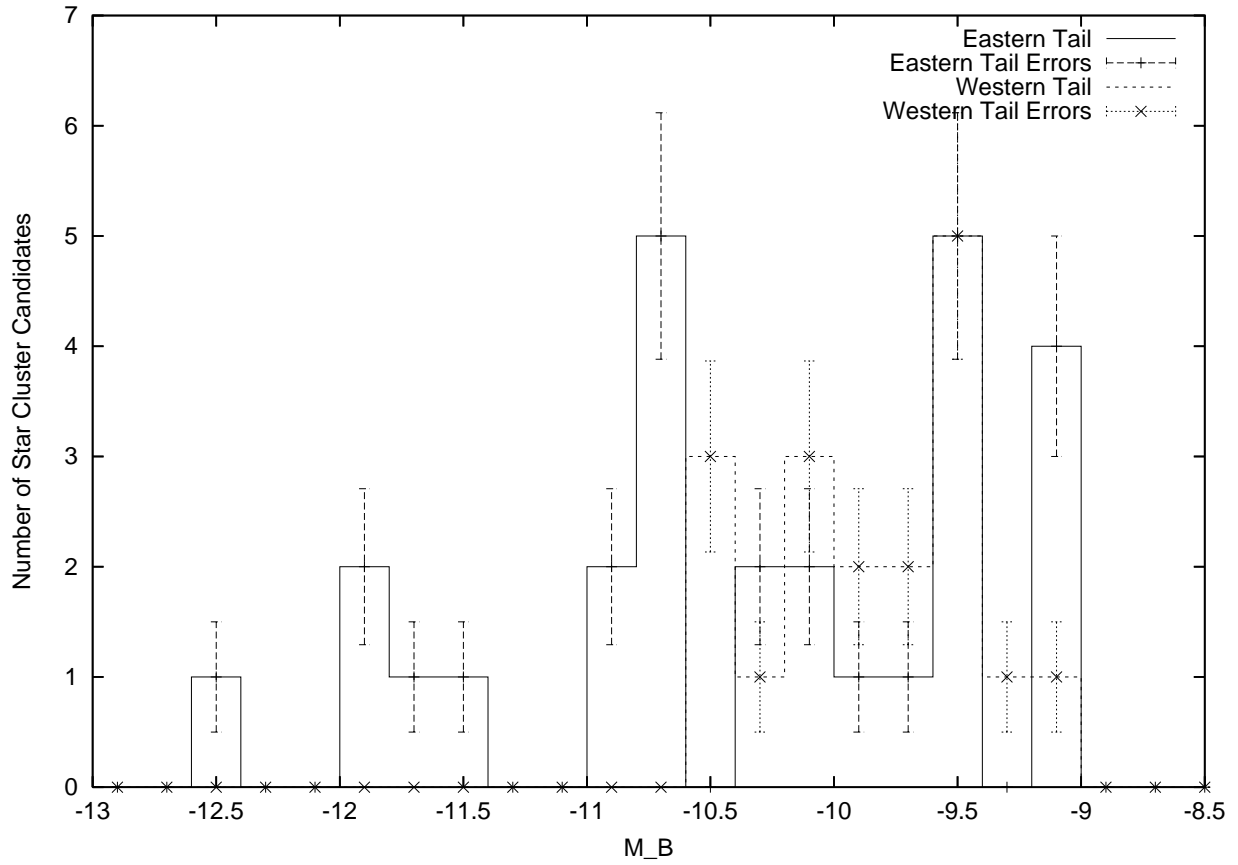


Fig. 7.— Histogram of M_B for final star cluster candidates. The solid line indicates Eastern tail candidates and the dotted line indicates Western tail candidates. Error bars represent the Poisson error for each bin: the square root of the number of star cluster candidates in the bin.

cluster in Orion which has $M_B = -4$. The B magnitude for 30 Dor in the Large Magellanic Cloud is $B = 9.63$ which at a distance of 50 kpc gives $M_B = -8.86$. So these star clusters are also more luminous than 30 Dor.

Since the Eastern tail has star cluster candidates with brightnesses similar to HII regions and our ground based observations may hide the extended nature of sources in the tidal tails, we examine the HST/WFPC2 images of both tails from Mullan et al. (2011). As shown in their Fig. 3.7 and Fig. 3.8, the brighter Eastern tail sources are extended with multiple bright clumps, but the Western tail sources remain compact and isolated. Therefore, our ground based observations of the Western tail sources are able to be treated as single star cluster candidate with one stellar population, particularly since the HST observations are only in F606W and F814W bands. However, we must treat the Eastern tail sources differently due to their extended nature.

Due to the compact and isolated nature of the Western tail sources, we continue with the 3DEF SED fitting method to determine ages, masses, and extinction for this tail. As shown in Figure 8, star cluster candidates in the Western tail tails have ages ranging from 2.5 Myr to 1 Gyr. The median age in the Western tail is 150 Myr. This tail has a significant fraction (90%) of star cluster candidates whose ages are less than the age of the merger ~ 200 Myr ($\log(\text{age}[\text{yr}]) = 8.3$). Therefore, there are star clusters that formed in situ in the Western tidal tail of NGC 2782. Figure 8 shows the range of star cluster candidate masses in the Western tail. The Western tail has star cluster candidates ranging in mass from $10^5 - 10^{7.25} M_\odot$, with a median mass of $5 \times 10^5 M_\odot$. The masses of the star cluster candidates in this tail are much larger than the $10^3 M_\odot$ of the Orion cluster and the $2 \times 10^4 M_\odot$ mass of R136, but are on the order of masses of star clusters in central starburst of the Antennae galaxy.

3.3. Star Cluster Complexes in Eastern Tail

Stars often form in pairs or clusters, not in isolation, and star clusters may also form in groups. These groups, called star cluster complexes, represent one of the levels of hierarchical star formation in galaxies and are often seen in spiral galaxies. In nearby spiral galaxies, Elmegreen & Salzer (1999) find a linear relation between the brightness of a star cluster complex and its linear size. In optical and molecular observations of M51, Bastian et al. (2005a) find that star cluster complexes are young (< 10 Myr) and have a strong correlation between mass and size (unlike for isolated star clusters) which is similar to that found for GMCs. In studies of Hickson Compact Group galaxies, Konstantopoulos et al. (2012) find a linear relation in HCG 59, but no relation for HCG 7 (Konstantopoulos et al. 2010).

Using the HST images from Mullan et al. (2011) and the methods of Konstantopoulos et al. (2010, 2012), we find the boundaries of these extended amorphous structures by eye measured by contours which are $> 10\sigma$ above the background (see Fig. 9). Photometry was performed on the polygonal apertures in the WF3 chip (the only one containing star cluster complexes in our tail region) using IRAF/POLYPHOT, zeropoints from Dolphin (2009), CTE correction for extended sources (Grogan et al. 2010), and foreground extinction from Schlafly & Finkbeiner (2011) and NED for the HST filters. We find 11 star cluster complexes in the Eastern Tail in the region between the main spiral and the putative dwarf galaxy. The size of each region was determined by taking the square root of the area contained in the polygonal aperture. Since the boundaries of the complexes were determined by eye, we estimate the error to be $\sim 10\%$ of the size of the complex. The sizes of the star cluster complexes ($0.19 < D < 0.63$ kpc) are consistent with sizes of star cluster complexes seen in nearby spiral galaxies (Elmegreen & Salzer 1999) and in compact groups (Konstantopoulos et al. 2010, 2012). As seen in Fig. 9, there is a linear relation between size versus luminosity (M_{V606}) for star cluster complexes in the Eastern tail. This indicates a uniform surface brightness for the star cluster complexes in the Eastern tail of NGC 2782. The properties of the star cluster complexes are shown in Table 6 which lists: ID number, associated star cluster candidate or HII region ID (if any), centroid pixel values, photometry for F606W and F814W bands and associated errors, $V_{606} - I_{814}$ color, size of the region as calculated above, and $M_{V,606}$. Of the 11 star cluster complexes, we find 6 of these have H α emission associated with them indicating ages < 10 Myr. All the complexes have blue color range of $-0.26 < V_{606} - I_{814} < 0.65$ also consistent with previous observations of star cluster complexes with HST (Konstantopoulos et al. 2010, 2012).

3.4. HII Regions

The H α observations yielded a detection of one source in the Western tail (previously published in Knierman et al. (2012); Werk et al. (2011); Bournaud et al. (2004); Torres-Flores et al. (2012) and six sources in the Eastern tail (see Figures 1 and 2 for location of sources). Previously, Smith et al. (1999) detected nine H α sources in the Eastern tail. Their observations were deeper than the ones presented here. Our detection limit for the Eastern tail is 7.7×10^{36} erg s $^{-1}$ and for the Western tail is 3.7×10^{37} erg s $^{-1}$. Table 7 lists the ID number of the star cluster candidate along with its letter designation from Smith et al. (1999) in the Eastern tail, tail inhabited, B magnitude, M_B magnitude, $U - B$, $B - V$, $V - R$, H α luminosity, and star formation rate (SFR) from the H α luminosity following Kennicutt (1998). One of our most luminous H α sources, E4, is coincident with the location indicated for the tidal dwarf galaxy candidate in Fig. 2 of Yoshida et al. (1994).

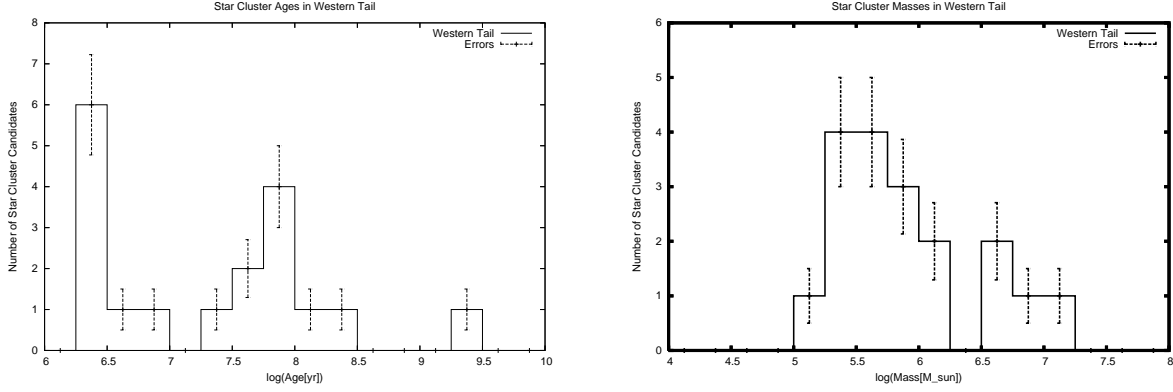


Fig. 8.— Left: Histogram of star cluster candidate ages for the Western tail of NGC 2782. Right: Histogram of star cluster candidate masses for the Western tail of NGC 2782. Error bars represent the Poisson error for each bin: the square root of the number of star cluster candidates in the bin.

Table 6. Properties of Star Cluster Complexes in the Eastern Tail of NGC 2782

ID	SCCID	X pixel	Y pixel	Area pixel ²	V_{606} mag	I_{814} mag	$V_{606} - I_{814}$ mag	Size kpc	$M_{V_{606}}$ mag
1	E0-A	164.75	637.25	345.5	22.284(0.036)	22.205(0.086)	0.079(0.093)	0.355(0.035)	-10.696(0.154)
2	E1-E	123.90	259.50	1192.0	20.927(0.019)	20.763(0.042)	0.164(0.046)	0.659(0.066)	-12.053(0.151)
3	E2-C	231.50	432.33	833.5	21.279(0.022)	21.057(0.047)	0.222(0.052)	0.551(0.055)	-11.701(0.152)
4	E3-F	399.20	276.60	486.5	22.323(0.043)	22.338(0.114)	-0.015(0.122)	0.421(0.042)	-10.657(0.156)
5	E4-H	240.83	200.50	98.0	23.052(0.041)	23.310(0.128)	-0.259(0.134)	0.189(0.019)	-9.928(0.156)
6	E356	151.27	235.73	1093.0	21.522(0.031)	21.083(0.054)	0.439(0.062)	0.631(0.063)	-11.458(0.153)
7	E530	76.67	547.50	824.5	21.650(0.030)	21.199(0.052)	0.451(0.060)	0.548(0.055)	-11.330(0.153)
8	E543	196.40	610.00	367.0	22.972(0.067)	22.321(0.098)	0.651(0.119)	0.365(0.037)	-10.008(0.164)
9	E555-B	71.67	599.00	869.0	20.979(0.018)	20.610(0.032)	0.369(0.037)	0.562(0.056)	-12.001(0.151)
10		181.40	136.40	224.5	23.019(0.056)	22.571(0.097)	0.449(0.112)	0.286(0.029)	-9.961(0.160)
11		226.75	655.50	392.5	23.207(0.085)	23.169(0.216)	0.038(0.232)	0.378(0.038)	-9.773(0.172)

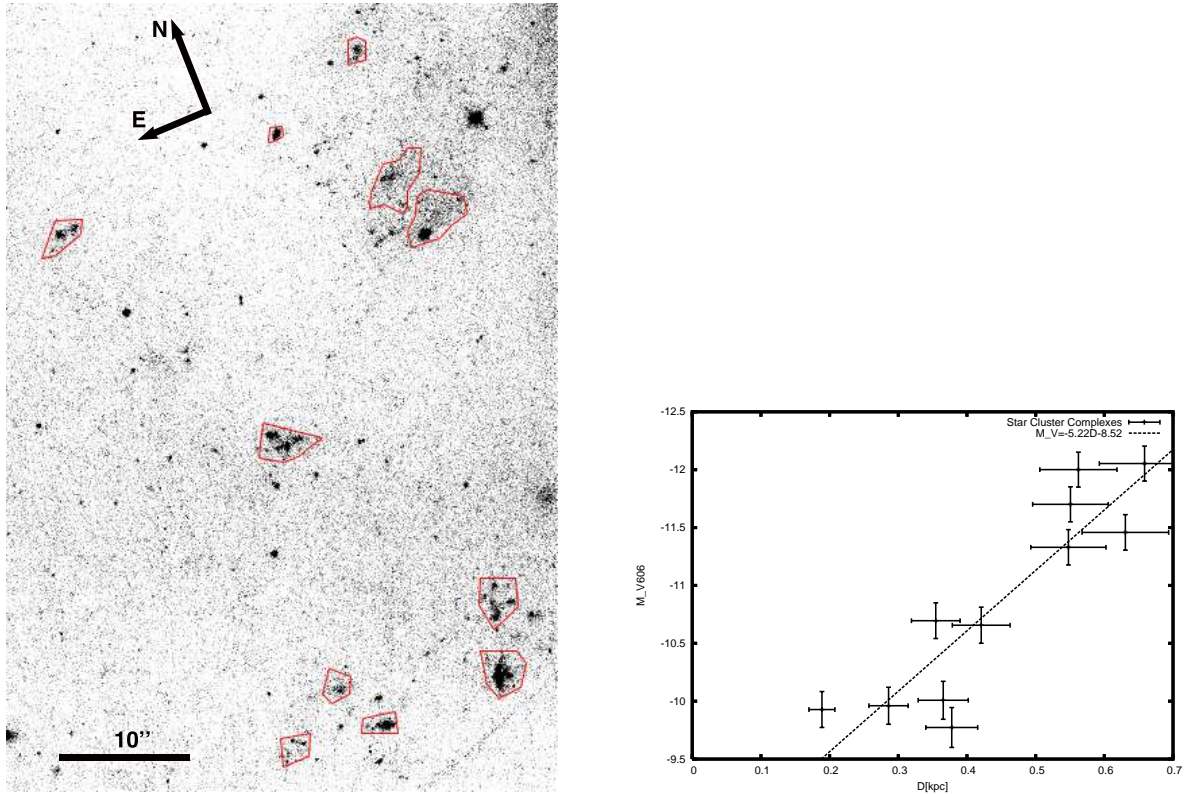


Fig. 9.— Left: HST/WFPC2 image in F606W of the Eastern tail of NGC 2782 from Mullan et al. (2011) with star cluster complexes marked in red. The area displayed here is the same as the inset in Fig. 1. Right: Size-luminosity diagram (D - M_{V606}) for star cluster complexes in the Eastern tail of NGC 2782. We find the star cluster complexes to follow a linear size-luminosity relation similar to complexes found in nearby spirals and in HCG 59.

In the Eastern tail, $L_{\text{H}\alpha} = 1.8 - 7.5 \times 10^{38} \text{ erg s}^{-1}$, while the HII region in the Western tail (previously reported in Knierman et al. (2012)) has $L_{\text{H}\alpha} = 19 \times 10^{38} \text{ erg s}^{-1}$. The Western tail HII region is listed in Torres-Flores et al. (2012) as System 6 which is the brightest of their young FUV sources in the Western tail. These luminosities are at least an order of magnitude less than those of the brightest HII regions in Sc galaxies ($L_{\text{H}\alpha} \sim 10^{40} \text{ erg s}^{-1}$), but are more typical of HII regions in Sa/b galaxies where the brightest ones are $L_{\text{H}\alpha} \sim 10^{39} \text{ erg s}^{-1}$. Both tails have HII regions fainter than 30 Dor which has $L_{\text{H}\alpha} = 6 \times 10^{39} \text{ erg s}^{-1}$, but brighter than Orion ($L_{\text{H}\alpha} = 10^{36} \text{ erg s}^{-1}$). In comparison with the tidal arm region of NGC 3077 (Walter, Martin, & Ott 2006), this very nearby tidal feature has 36 HII regions with a total $L_{\text{H}\alpha} = 2.9 \times 10^{38} \text{ erg s}^{-1}$ which is similar to E3 and E4 and lower than W235. The $\text{H}\alpha$ region in the Western tail has blue colors and a young age fit with the 3DEF models. Given their $\text{H}\alpha$ emission, these 7 sources are likely to be less than 10 Myr old indicating star formation in situ in both tidal tails.

3.5. Comparison to other star cluster populations in tidal debris

In comparing NGC 2782 with the tidal debris of minor merger NGC 6872 (Bastian et al. 2005b), we find that both star cluster systems have similar ages ($\sim 10 - 100 \text{ Myr}$). However, NGC 6872 has more luminous star clusters ($\langle M_V \rangle = -12.2$) than NGC 2782 ($\langle M_{V,East} \rangle = -11$; $\langle M_{V,West} \rangle = -10$). The difference in star formation can be seen in comparisons of $\text{H}\alpha$ maps of both systems. NGC 6872 has widespread $\text{H}\alpha$ emission along both tails (Mihos et al. 1993) which are correlated with young massive star clusters (Bastian et al. 2005b). On the other hand, NGC 2782 has only a few discrete $\text{H}\alpha$ emission regions in the Eastern tail, and only one in the Western tail. NGC 6872 has a slightly younger age ($\sim 145 \text{ Myr}$) than NGC 2782 perhaps accounting for the difference in star formation in the tidal tails. There may also be differences in the progenitor galaxies; these could account for differences in star formation rate of the tidal tails. NGC 2782 is a strongly star forming galaxy while NGC 6872 has little star formation in its central regions. The NGC 6872 interaction likely stripped off gas-rich outer layers of the large spiral galaxy like the Western tail of NGC 2782 while the Eastern tail of NGC 2782 may be remnants of the smaller galaxy. The sample of minor mergers by Ferreiro, Pastoriza, & Ricketts (2008) include larger structures detected by $\text{H}\alpha$ emission, leading to younger and more massive structures such as HII regions and Tidal Dwarf Galaxies with very few star clusters detected.

The star clusters in the tidal tails of major merger NGC 3256 (Knierman et al. 2003) have similar ages (30-300 Myr) and luminosities ($\langle M_V \rangle \sim -10$) to those in NGC 2782. Three star clusters in the Western Tail of NGC 3256 were spectroscopically confirmed by

Trancho et al. (2007) at Gemini South. From their GMOS-S spectra, they determine ages to be ~ 80 Myr for two star clusters and ~ 200 Myr for the third having approximately solar metallicities. The three star clusters in the Western tail of NGC 3256 have masses ($1 - 2 \times 10^5 M_{\odot}$) which are similar to the average masses of star clusters in the Western tail of NGC 2782. Using the HST/WFPC2 images of the Western tail of NGC 3256, Trancho et al. (2007) show the three star clusters to have a large size ($r_{eff} \sim 10 - 20$ pc) compared to Milky Way globular clusters or other young massive clusters ($r_{eff} \sim 3 - 4$ pc). The large size of the star clusters may mean that the GMC underwent weak compression during the star cluster formation. On the other hand, the tidal tail star clusters may not have experienced the tidal stripping that other young clusters in the centers of galaxies have.

3.6. Comparing Gas Properties of the Tails

We now examine the gas properties of these two tails. Both tails have been previously observed in HI (Smith 1994) and in CO (Smith et al. 1999; Braine et al. 2001). The Eastern tail is rich in both HI and CO while the Western tail has HI, but no detectable CO. Table 8 lists the location, area, SFR density (Σ_{SFR}) from [CII], SFR density (Σ_{SFR}) from H α , mass of HI, molecular gas mass, total gas surface density, and predicted star formation rate density from the gas density from Kennicutt (1998). This table includes information for the local regions within each tail as well as for the entire tail.

3.6.1. Neutral Hydrogen - HI

There are 3 massive HI clumps in both tails which have star cluster candidates associated with them. In the Western tail, Smith (1994) measure 10 massive HI clumps. These range in masses from $3 \times 10^7 M_{\odot}$ to $1.8 \times 10^8 M_{\odot}$. Only three of these massive HI clumps have star cluster candidates found within their bounds. Since only one HII region was found in the Western tail, we use the H α background limit as a limit for the H α star formation rate for the other two HI clumps. The magenta boxes in Fig. 2 show the location of these three clumps in the Western tail. In the Eastern tail, individual clumps are not tabulated in Smith (1994), but their masses and sizes were determined by inspection of their map of HI contours. We also include a box of the area surrounding the tidal dwarf galaxy candidate (TDGC) found by Yoshida et al. (1994) even though it falls outside the HI peaks. The HI clumps in the Eastern tail have masses from $3 - 8 \times 10^8 M_{\odot}$, but only $4 \times 10^7 M_{\odot}$ for the location of TDGC. The four regions in the Eastern tail have H α sources which provide the local H α luminosities. If more than one HII region resides in a box, we sum the luminosities

Table 7. Properties of $H\alpha$ sources in Tidal Tails of NGC 2782

Number	Tail	B mag	M_B mag	U-B mag	B-V mag	V-R mag	$L_{H\alpha}$ 10^{38}erg s^{-1}	SFR($H\alpha$) $M_{\odot}\text{ yr}^{-1}$
E0-A ^a	E	20.98	-11.95	-0.49	0.79	0.52	6.5(0.9)	0.0051(0.0008)
E1-E ^a	E	21.57	-11.37	0.12	0.23	0.38	7.5(1.0)	0.0059(0.0009)
E2-C ^a	E	21.17	-11.76	0.01	0.17	0.59	1.8(0.4)	0.0015(0.0003)
E3-F ^a	E	21.60	-11.33	-0.20	0.51	-0.28	2.7(0.5)	0.0022(0.0004)
E4-H ^a	E	21.92	-11.18	-0.01	-0.76	0.97	2.7(0.5)	0.0022(0.0004)
E555-B ^a	E	20.996	-11.994	-0.138	0.417	0.222	6.0(0.9)	0.0047(0.0007)
W235	W	22.492	-10.498	-0.60	0.42	0.33	19(3)	0.015(0.002)

(a) Letter Nomenclature from Smith et al. (1999)

Table 8. Comparison of Local & Global Star Formation Rates

Location	ID	Area kpc^2	$\Sigma_{\text{SFR}}([\text{CII}])$ $10^{-3}M_{\odot}yr^{-1}kpc^{-2}$	$\Sigma_{\text{SFR}}(H\alpha)$ $10^{-3}M_{\odot}yr^{-1}kpc^{-2}$	M_{HI}^a 10^8M_{\odot}	M_{mol}^b 10^8M_{\odot}	Σ_{gas}^c $M_{\odot}pc^{-2}$	$\Sigma_{\text{SFR}}(\text{gas})^d$ $10^{-3}M_{\odot}yr^{-1}kpc^{-2}$
East								
TDGC	E1,E4	7.09	4.5(0.2)	1.1(0.1)	0.4	2.6 ^f	44	51
HI-N	E3	11.8	< 0.3	0.27(0.04)	5.2	2.6 ^f	82	119
HI-M	E2	7.09	2.5(0.3)	0.22(0.05)	3.1	3.69(0.09)	112	184
HI-S	E0,E555	23.6	2.9(0.1)	0.42(0.03)	8.1	3.8 ^f	62	82
E Tail		3000	0.04	0.01	17	8.6	1.1	0.3
West								
HI-N		8.6		< 0.03	0.73	< 0.086 ^e	< 12.5	< 9
HI-M	W235	14.7	< 1.1	1.0(0.2)	1.15	< 0.22	< 9.1	< 5
HI-S		19.3		< 0.02	1.16	< 1.5 ^f	< 10.1	< 6
W Tail		2300		0.009	19	< 1.8	< 1.6	< 0.5

^aSmith (1994), corrected for distance

^b M_{mol} inferred from CO observations

^cIncludes helium ($M_{\text{gas}} = 1.36(M_{\text{HI}} + M_{\text{H}_2})$)

^dFrom Kennicutt (1998), Σ_{gas} includes only HI and H₂

^eBraine et al. (2001), corrected for distance

^fSmith et al. (1999), corrected for distance, TDGC and E-HI-N use Far-Far-East pointing while E-HI-S uses South-Far-Far-East pointing.

of the regions. The total $H\alpha$ luminosity for each region is presented in Table 9. We find that TDGC now has the highest $L_{H\alpha}$ in the Eastern tail, however, the Western tail HII region remains the brightest. The magenta boxes in Fig. 1 show the location of these four areas in the Eastern tail.

3.6.2. Cold Molecular Gas - CO

Smith et al. (1999) used the Kitt Peak 12 meter to look for CO(1-0) in NGC 2782. They used a grid pattern with $25''$ spacing and detect CO in 5 out of 6 pointings in the Eastern tail region. These locations are shown as asterisks in Figure 4. Only 2 pointings (Far-Far-East and South-Far-Far-East) are located in the same region as the Herschel PACS observations. To correlate the Herschel PACS observations more accurately with molecular observations, we made new observations with the Kitt Peak 12 meter at the same location. The Eastern tail location was detected at a lower signal-to-noise (about 4σ , see Fig. 6) than previous observations, but has the same velocity as the areas observed in the Eastern tail by Smith et al. (1999). Assuming the source fills the beam (a coupling efficiency of $\eta_c = 0.64$) and a Milky Way X_{CO} , the molecular mass observed at the same location as the Herschel PACS observations is $M_{mol} = 3.69 \pm 0.09 \times 10^8 M_{\odot}$.

In the Western tail, Smith et al. (1999) looked for CO at two locations, the northern and southern HI clumps, but did not detect any CO(1-0) emission. The HII region in the Western tail Knierman et al. (2012) is located $\sim 20''$ away from the location where Smith et al. (1999) searched for CO(1-0), so we made deeper observations at this location. The Western tail location, coincident with the $H\alpha$ source (Knierman et al. 2012), remains undetected in CO(1-0) with an upper limit of $M_{mol} < 0.22 \times 10^8 M_{\odot}$. Braine et al. (2001) reobserved the northern clump with IRAM, but still did not detect CO. Table 8 lists the molecular gas mass or upper limits from these pointings.

The use of the standard Milky Way X_{CO} is not without precedence for tidal debris regions even though major merger TDGs have been observed to have $\sim 0.3Z_{\odot}$ since they are pulled from the outer regions of spiral galaxies (Duc, Bournaud, & Masset 2004). The previous observations of the tidal debris of NGC 2782 by Smith et al. (1999) use the Milky Way conversion factor for ease of comparison with other observations. In Boquien et al. (2011) and Walter, Martin, & Ott (2006), the standard Milky Way CO to H_2 conversion factor ($X_{CO} = 2 \times 10^{20} \text{ cm}^{-2} (\text{K km s}^{-1})^{-1}$ or $(\alpha_{CO1-0} = 4.3 M_{\odot} (\text{K km s}^{-1} \text{ pc}^2)^{-1})$) was used. However, as mentioned in Knierman et al. (2012), X_{CO} has a strong dependence at low metallicities (Leroy et al. 2011; Genzel et al. 2012). At a metallicity of $0.3Z_{\odot}$ (or $\mu_0 = 8.19$), the conversion factor is $\alpha_{CO1-0} = 27.5 M_{\odot} (\text{K km s}^{-1} \text{ pc}^2)^{-1}$ and gives a factor of

6 higher molecular mass limit ($M_{\text{mol}} \leq 1.2 \times 10^8 M_{\odot}$) than that from the standard conversion factor ($M_{\text{mol}} \leq 2 \times 10^7 M_{\odot}$).

3.6.3. *Herschel/PACS observations of [CII]*

Observations of [CII] with Herschel/PACS show two major peaks in the Eastern tail (Fig. 4), but no detection in the Western tail. The peaks in the Eastern tail correspond with the two strongest $H\alpha$ sources, E0 and E1. The northern peak in [CII] (TDGC) is near E1 (the location indicated for the TDGC (Yoshida et al. 1994)) and E4. The southern peak (E-HI-S) is near the brightest $H\alpha$ source, E0, and the HI peak in the Eastern tail. A secondary peak of [CII] in this area is near the $H\alpha$ source E555-B. The locations where spectra were extracted are indicated in Figure 4 with the spectra shown in Figure 5. As above, the extracted spectra were summed, multiplied by the bandwidth (745.96 MHz) and the flux correction factor for a single pixel (2.0), and converted to cgs units by the conversion factor of $10^{-23} \text{ erg s}^{-1} \text{ cm}^{-2}$. We multiply the flux by $4\pi D^2$ to calculate the luminosity. To calculate $I_{[\text{CII}]}$, we divide the flux by the circular beam size of $12'$. For each location, Table 9 lists the location, coordinates, luminosity of [CII], luminosity of $H\alpha$, I_{CO} from this work or for the nearest location observed by Smith et al. (1999), $I_{[\text{CII}]} / I_{\text{CO}}$, the SFR from [CII] calculated using the relation from Boselli et al. (2002), and SFR from $H\alpha$ using Kennicutt (1998). Included in the table are limits for the regions with no strong detections.

The southern source, E-HI-S, is 1.1 times brighter than the TDGC source and has a luminosity of $15.1 \pm 0.6 \times 10^{38} \text{ erg s}^{-1}$. E-HI-S is similar in brightness to its neighbor, B, though some of the [CII] flux near B could be off the array. So this observation may be a lower limit. We extract a spectrum at the location of the $H\alpha$ source, E2-C or E-HI-mid, even though no peak is observed in the line intensity map. Since there is [CII] emission there at a level of $4\text{-}5\sigma$, we detect a line with luminosity less than half the value of E-HI-S. We also extract a spectrum near the location of the northeast $H\alpha$ source, E3/E-HI-N, where there is no [CII] emission detected. The Western tail has an upper limit of $< 0.6 \times 10^{38} \text{ erg s}^{-1}$.

To calculate the SFR from [CII], we need to correct the line luminosity to account for contamination from the warm ionized medium. Boselli et al. (2002) cite that 2/3 of the [CII] flux comes from the neutral medium based on theoretical predictions. Based on models of HII regions, Mookerjee et al. (2011) use 70% of the [CII] from the neutral medium for their calculations which is consistent with their non-detection of the [NII] $205\mu\text{m}$ line from BCLMP 302 in M33. The first observational determination of the fraction of [CII] flux from the neutral medium is from Oberst et al. (2006). They use the first detection of the [NII] $205\mu\text{m}$ line and show that 27% of the [CII] line flux should come from the warm ionized

medium, leaving 73% of [CII] to come from the neutral medium. While the tidal tails of NGC 2782 may be different from the Carina nebula observed by Oberst et al. (2006), we adopt the Oberst et al. (2006) value for our determination of SFR from [CII] emission due to the paucity of observations of the [NII] 205 μ m line. To calculate SFR from [CII], we multiply the [CII] flux by 0.73 (Oberst et al. 2006) and use Eq. 3 from Boselli et al. (2002) who observe nearby late-type galaxies in H α and [CII].

4. Discussion

Based on the observations described above, we find both tidal tails of NGC 2782 host young star forming regions that formed within the tidal tail. The Eastern tail has more luminous star clusters which are hosted in larger star cluster complexes whereas the Western tail has only isolated star clusters. Therefore, packaging of star formation is different between the tails. The Eastern tail also has CO and [CII] emission, whereas the Western tail has non-detections. The HII region in the Western tail is more luminous than any single HII region in the Eastern tail, so the difference between the tails is not simply that the Western tail is forming stars at a lower level than the Eastern tail. To determine what might be causing these differences between two tidal tails of the same system, we compare the following properties: ambient pressure, gas phase, amount of gas, and efficiency of star formation.

4.1. Ambient Pressure

The difference in star formation modes between the tails could be due to a differing initial distribution of star cluster masses. Differences in cluster initial mass function (CIMF) are difficult to determine since it is hard to find young star cluster populations that have not experienced significant evolution. A few studies have attempted determining the CIMF (Portegies Zwart, McMillan, & Gieles 2010). The CIMF is generally described like a Schechter distribution

$$\frac{dN}{dM} = AM^{-\beta} \exp(-M/M_*) \quad (3)$$

with $\beta \sim 2$ and M_* indicating the mass at which the change in the slope of the mass function occurs. For spiral galaxies like the Milky Way, $M_* \sim 2 \times 10^5 M_\odot$, but interacting galaxies like the Antennae show $M_* > 10^6 M_\odot$ (Portegies Zwart, McMillan, & Gieles 2010). Therefore, the environment where star cluster formation occurs seems to affect the CIMF and, in particular, the value of M_* .

This possible difference in CIMF between the tails might be due to the difference in the spatial arrangement of molecular gas. Forming stars tend to destroy their parent molecular environment, leaving behind clumpy remnants of molecular material. Beam dilution may render the CO unobservable even with moderate resolution ($< 1'$) like the CO observations of the HI peaks in the Western tail Smith et al. (1999) and Braine et al. (2001). With the concentration of molecular gas in small clumps, the tail may have produced correspondingly lower mass star clusters.

A second possibility for the difference in CIMF could be due to a lower metallicity. With a lower metallicity there would be less carbon and oxygen to make CO so we may not detect it. However, why a lower metallicity environment would make lower mass clusters is an open question.

A third possibility for the difference in CIMF between the tails could be due to the environment. The ambient pressure in the Western tail could be lower than in the Eastern tail which would lower the star formation rate (Blitz & Rosolowsky 2006), possibly making lower mass star clusters. Even for solar metallicities, when the ambient pressure is low, CO will form deeper within the dense star forming cloud.

We examine the third possibility next. The locations and masses of GMCs are likely to be regulated by the structure of the HI from which the GMC formed, particularly in galaxies which are dominated by atomic gas (Blitz & Rosolowsky 2006). In particular, M33 shows this correlation between its GMCs and peaks in the HI gas (Rosolowsky et al. 2007).

While Braine et al. (2001) stated that the lack of CO down to sensitive limits at places of high column density HI indicated that the Western tail is not gravitationally bound and so the gas has not collapsed to form H_2 and hence new stars, the observations presented here show that new star clusters are being formed in the tail. Based upon HI peaks in the Western tail of NGC 2782, GMCs are expected to be at those locations. The largest size of the molecular cloud that one would expect to be associated with the HI clump can be estimated using the formulation for M_{char} of Elmegreen, Kaufman, & Thomasson (1993):

$$M_{char} = \pi l_{min} c_g \sqrt{\frac{\mu}{2G}} \quad (4)$$

where c_g is the velocity dispersion of the gas in 3-D, μ is the mass per unit length of the cloud (M/l_{max}), and l_{min} and l_{max} are the minor and major axes of the HI cloud. This equation gives the characteristic mass of a “supercloud” using the size, mass, and velocity dispersion of the HI clump. This supercloud is the overall entity which becomes self-gravitating and the GMCs collapse to form inside this supercloud by turbulent fragmentation.

Table 10 has the M_{HI} , velocity dispersion, size and resulting M_{char} for 3 HI clumps in the Eastern tail and 3 HI clumps in the Western tail. Smith (1994) measured 10 HI clumps in the Western tail, but the 3 presented here are ones with star cluster candidates at that location. The M_{char} for the Eastern Tail clumps ranges from $9.5 - 18 \times 10^8 M_{\odot}$ while the Western tail is slightly smaller with a range from $6.6 - 11 \times 10^8 M_{\odot}$.

While M_{char} does not predict an exact mass for a GMC, this does indicate that similar masses of GMCs are expected in both the Eastern and Western tails. However, no molecular gas was observed in the Western tail down to a limit two orders of magnitude below M_{char} . A massive HI clump in the NW tidal tail of NGC 7252 has $M_{\text{char}} \sim 3.3 \times 10^9 M_{\odot}$. This clump, as shown in Table 10, has more HI than those in NGC 2782 and molecular gas of $2 \times 10^7 M_{\odot}$.

That the Western tail lacks molecular gas at the locations of high HI column density could be due to either its absence or its inobservability. In the less dense region of the Western tail, even a small amount of star formation could have destroyed the molecular gas there. The Eastern tail is more dense and so its molecular gas would not be destroyed as easily. If the molecular gas is not entirely destroyed by the radiation of young stars, it could exist instead in smaller clouds which would be greatly affected by beam dilution with single dish telescopes (beam sizes of $22''$ to $1'$).

4.2. Gas Phase

We examine whether the lack of massive star clusters and star cluster complexes in the Western tail is related to the properties of the ISM in the tidal tail. To do this, we look at various tracers of the reservoir of gas available for star formation in both tails on both local and global scales. We first compare neutral hydrogen gas to molecular gas traced by CO emission. Then we compare neutral hydrogen to ionized gas traced by [CII] emission. Finally, we compare molecular gas traced by CO emission to ionized gas traced by [CII] emission.

Comparing the CO and HI mass ratio, we find the highest to be TDGC ($M_{\text{H}_2}/M_{\text{HI}} = 6$) the other three regions have ratios of 0.5, 1, and 0.5 for the north, mid, and south regions, respectively. In the Western tail, we find $M_{\text{H}_2}/M_{\text{HI}} < 0.2$. This indicates that there is less CO in the Western tail for the HI mass as compared to the Eastern tail on local scales.

We next compare the [CII] to HI. In Fig. 16 of Stacey et al. (1991), they plot the expected [CII] line flux for given HI column densities for various phases of the ISM in the infinite temperature limit. The galaxies of their sample lie about 2 dex above the lines for

Table 9. [CII] and H α Observations of Regions in Eastern and Western Tails

Location	H α ID	RA	Dec	$L_{[CII]}$ 10^{38} erg s $^{-1}$	$L_{H\alpha}$ 10^{38} erg s $^{-1}$	I_{CO} K km s $^{-1}$	$I_{[CII]}/I_{CO}^b$	$SFR([CII])^b$ $M_{\odot}yr^{-1}$	$SFR(H\alpha)^c$ $M_{\odot}yr^{-1}$
East									
TDGC	E1,E4	9:14:10.92	+40:06:48.8	13.4(0.6)	10(1.2)	0.39(0.06) ^a	2950	0.032(0.001)	0.008(0.001)
E-HI-N	E3	9:14:12.46	+40:06:50.6	<0.9	4.1(0.6)	0.39(0.06) ^a	<190	<0.004	0.0032(0.0005)
E-HI-M	E2	9:14:11.46	+40:06:35.6	6.3(0.7)	2.0(0.4)	0.43(0.05)	1840	0.0170(0.005)	0.0016(0.0003)
E-HI-S	E0	9:14:11.26	+40:06:20.6	15.1(0.6)	6.7(0.9)	0.57(0.08) ^a	4860	0.0347(0.001)	0.0053(0.0007)
E-HI-S-B	E555	9:14:10.66	+40:06:26.6	>14.1(0.7) ^f	6.0(0.9)	0.57(0.08) ^a	4520	>0.033(0.002)	0.0047(0.0007)
Total ^e	all	9:14:10.63	+40:06:41.6	77(2)	29(2)	0.43(0.05)	> 1148	0.125(0.003)	0.023(0.002)
West									
W-HI-M	W235	9:13:51.2	+40:08:07	<5.6	19(3)	<0.02	<35200	<0.02	0.015(0.002)

^aSmith et al. (1999)

^b1 K km s $^{-1}$ = 1.6×10^{-9} erg s $^{-1}$ cm $^{-2}$ sr $^{-1}$ (Stacey et al. 1991)

^cUsing equation from Boselli et al. (2002)

^dUsing equation from Kennicutt (1998)

^eTotal of the area of the Herschel/PACS spectral observations.

^fThis is a lower limit since source is at the edge of the array.

Table 10. Characteristic Sizes of HI Clumps in the Tidal Tails of NGC 2782

Location	σ_v^a (km/s)	l_{min} (kpc)	l_{max} (kpc)	M_{HI}^a ($10^8 M_{\odot}$)	M_{char} ($10^8 M_{\odot}$)	Observed M_{mol} ($10^8 M_{\odot}$)
E-HI-N	30	2.96	2.96	3.85	15.3	2.6(0.5) ^b
E-HI-M	40	1.78	2.96	2.31	9.50	3.69(0.09)
E-HI-S	40	2.96	5.92	6.02	18.1	3.8(0.5) ^b
W-HI-N	49	2.10	3.05	0.54	6.56	< 0.086 ^c
W-HI-M	35	5.67	7.56	1.00	10.9	< 0.22
W-HI-S	30	3.78	3.78	0.86	8.19	< 1.5 ^b
N7252 TDG	31	5.00	5.00	10	33.2	0.2

^a(Smith 1994; Smith et al. 1999)

^b(Smith et al. 1999)

^b(Braine et al. 2001)

“standard” H I clouds and the intercloud medium. In direct comparison to their galaxies and Galactic H II regions, the local regions in the Eastern and Western tail of NGC 2782 are deficient in [C II] by about 2 dex. The Eastern tail has an average H I column density of $6 \times 10^{20} \text{ cm}^{-2}$, with a peak of $1.75 \times 10^{21} \text{ cm}^{-2}$ in the E-HI-S region. For a “standard” H I cloud ($n_H \sim 30 \text{ cm}^{-3}$), the peak column density in the Eastern tail predicts $I_{[\text{C II}]} \sim 5 \times 10^{-6} \text{ erg s}^{-1} \text{ cm}^{-2} \text{ sr}^{-1}$ which is a factor of 1.6 larger than that observed in E-HI-S. If we consider the average H I column density for the Eastern tail, then $I_{[\text{C II}]} \sim 2 \times 10^{-6} \text{ erg s}^{-1} \text{ cm}^{-2} \text{ sr}^{-1}$ which is similar to the values observed for the Eastern tail. In the Western tail, the H I column density is $\sim 1 \times 10^{21} \text{ cm}^{-2}$ and the predicted value for $I_{[\text{C II}]}$ is a few times the observed upper limit for [C II].

To directly compare [C II] to CO, we determine the ratio of their intensities. Our values for $I_{[\text{C II}]}$ are calculated by dividing the flux of [C II] by the beam size (a HPBW of $12''$). As shown in Table 9, we observe the $I_{[\text{C II}]} / I_{\text{CO}}$ ratio to range from 1840-4860 for those where both [C II] and CO are detected. This is at the lower end of the values for most of the normal and starburst galaxies observed Stacey et al. (1991) and aligns more with the values for Galactic H II regions and molecular clouds. Stacey et al. (1991) found that there was a constant ratio between [C II] and CO fluxes for starburst and Galactic OB star forming regions ($I_{[\text{C II}]} / I_{\text{CO}} = 6300$). The ratio for TDGC is 2950 and the ratio for E-HI-S is 4860. These values are a few times lower than the constant ratio. The limit for the Western tail gives a $I_{[\text{C II}]} / I_{\text{CO}} > 35200$. Stacey et al. (1991) finds the ratio to be lower for non-OB star forming regions in the Milky Way and normal galaxies with lower dust temperatures and those ratios range from 4400 to as low as 900 which match with our observations in the Eastern tail. Our limit in the Western tail is larger than the constant ratio from Stacey et al. (1991) and is more similar to their value for 30 Dor in the LMC ($I_{[\text{C II}]} / I_{\text{CO}} = 40,000$) which is also an area of lower metallicity than most of their other observed regions. If we compare to the more recent observations of area of the H II region BCLMP 302 in M33 Mookerjee et al. (2011), we find our values align to their range of ratios from 1000 – 70,000 shown in Fig. 12 of their erratum. For the H II region BCLMP 302 itself, the values of $I_{[\text{C II}]} / I_{\text{CO}}$ range from 6000 – 30,000 which are higher than our ratios for the Eastern tail, but have an upper end similar to the limit for the Western tail H II region. The H II region BCLMP 302 in M33 has a $L_{\text{H}\alpha} = 2.2 \times 10^{38} \text{ erg s}^{-1}$ which is similar to the H II regions in the Eastern tail. However, the [C II] intensity in BCLMP 302 is 28 times lower in the Eastern tail and 84 times lower than the Western tail limit.

There may be a mismatch between the CO observations and the [C II] peaks from the different beam sizes of the two instruments. PACS spectrometer has a beam with half power beam width (HPBW) of $12''$ at $159 \mu\text{m}$ while the CO data are from the Kitt Peak 12 meter

which has a beam with FWHM of $55''$. We instead extract [CII] spectra from the PACS array by summing the flux from the whole array to better match the CO beam and by dividing the flux by the area of the array ($47'' \times 47''$). This is indicated in Table 9 as “Total”. Even with summing the flux from the whole PACS array, the CO observations still have a larger beam size which means we have a lower limit on the ratio of $I_{[\text{CII}]} / I_{\text{CO}} > 1148$.

In either case, it appears that the Eastern tail has a deficiency of [CII] since the $I_{[\text{CII}]} / I_{\text{CO}}$ ratio is on the low end of regions previously observed. And given that this is among the first tidal tail region to be observed in [CII], having a lower value for $I_{[\text{CII}]} / I_{\text{CO}}$ may not be surprising.

4.2.1. *Non-detection of [CII] in the Western tail*

Given the non-detection of CO in the Western tail, we might expect the molecular gas to be in another form. CO does not form until and A_V of 3 or more, while H_2 forms at A_V of less than 1 (Hollenbach & Tielens 1997). In a low pressure environment like a tidal tail a substantial amount of molecular gas can exist with conditions that do not favor the formation of CO, so the CO to H_2 conversion factor is not a constant. In the low gas density environment of tidal debris a substantial reservoir of molecular gas can exist at low A_V that will not be detectable through CO. However, in this regime, C^+ will be present in higher amounts. Theoretical models for molecular clouds in Wolfire, Hollenbach, & McKee (2010) show that the fraction of molecular mass in the “dark gas” (H_2 and C^+) is $f \sim 0.3$ for typical galactic molecular clouds. For lower A_V and lower metallicities (as in these tidal tail regions), the fraction of dark mass in H_2 increases. Given this reason, we observed the Western tail with Herschel to see if [CII] was present where CO was not.

We do not find [CII] in the Western tail at the location of the HII region at a significant level. This HII region has a higher $\text{H}\alpha$ luminosity than any individual HII region in the Eastern tail, but [CII] emission is only detected in the Eastern tail. Given that $\text{H}\alpha$ and [CII] emission ultimately originate from the same sources of hard UV photons with energy greater than 13.8 eV, they are expected to trace each other. In BCLMP 302 in M33, Mookerjea et al. (2011) find [CII] emission 84 times greater than the Western tail limit, even though it has an $\text{H}\alpha$ luminosity 9 times less than the Western tail.

If carbon was not available to be ionized, the most likely place for it to be is in CO. However, the Western tail has no detected CO at this location. From the calculations of the characteristic mass in Section 4.2 of the paper, we expect the largest size of the molecular cloud mass to be $\sim 1 \times 10^9 M_\odot$, but the upper limit for this region is $0.2 \times 10^8 M_\odot$. (in the

Eastern tail, M_{char} is $\sim 3 - 5$ times the observed value of M_{mol} , so the factor of 54 between M_{char} and the upper limit on molecular mass in the Western tail is significant). The lack of [CII] and CO emission would then indicate that this HII region is likely to have a low carbon abundance. However, previous emission line spectra of this HII region (Torres-Flores et al. 2012; Werk et al. 2011) from Gemini have shown that it has a metallicity greater than solar. This seems to be at odds with the non-detections of [CII] and CO in the Western tail. However, Torres-Flores et al. (2012) use nebular oxygen emission for their metallicity determination. It is possible for this to be compatible with a low carbon abundance and a very low C/O ratio. Oxygen is the most common element produced in core collapse supernovae events whereas carbon is produced in relatively small amounts. The source of most carbon in the ISM is AGB stars. If this material has been primarily enriched by recent star formation, it is possible to build up a high abundance of oxygen and alpha elements without producing a significant enhancement of carbon and also iron. The age of the Western tail is about 200-300 Myr and so in situ star formation in the tail is unlikely to have synthesized large quantities of carbon (Arnett 1996).

Also, molecular gas may have been dissociated by a high UV flux in this region, associated with the most massive stars in the star cluster. FUV-NUV color from *GALEX* observations by Torres-Flores et al. (2012) show that this region show a FUV-NUV color of -0.14 mag. For a simple Salpeter IMF of $dN/dM = cM^{-(1+x)}$ with $x=1.35$, a $10^{5.35} M_{\odot}$ cluster contains 1660 stars of $8 M_{\odot}$ or greater. Even for an extreme value of $x=2.35$, there are still 40 stars of 8 or more M_{\odot} . This provides sufficient UV flux to photodissociate H_2 out to several hundred parsecs, comparable to the size of the Orion Molecular Cloud Complex. It is therefore unlikely that molecular gas has long lifetimes unless present at high densities, as in the Eastern tail of NGC 2782.

4.3. Star Formation in Tidal Debris

To consider whether the difference in star formation modes between the two tails is due to the amount of gas present for star formation, in each tail we calculate the star formation rates per unit area from the $H\alpha$ luminosity and also from [CII] luminosities and compare these to the predicted SFR from the gas surface density. This is done for global values of the tidal tails as well as locally over HI clumps in both tails.

4.3.1. Star Formation on Global Scales

Using the entire tail areas as calculated above, we find the SFR and SFR per area (Σ_{SFR}) for both tails. In Table 8, the global properties of Σ_{SFR} from [CII], from the $H\alpha$ luminosity, and the total gas surface density (including both HI and molecular gas) are listed for each tail. For this calculation we use the $L_{H\alpha}$ from Smith et al. (1999) since they detected fainter $H\alpha$ emission than these observations. In the Eastern tail the $\Sigma_{SFR}(H\alpha)$ is an order of magnitude below the expected value of $\Sigma_{SFR}(gas)$. In the Western tail, $\Sigma_{SFR}(H\alpha)$ is two orders of magnitude below the expected value from the gas density.

Using the summed flux over the entire PACS spectroscopy array, as described above and equation for SFR from [CII] in Boselli et al. (2002), we calculate the Global SFR ([CII]) for the Eastern tail to be $0.125 M_{\odot} \text{ yr}^{-1}$. If we assume that the flux detected by the PACS pointing is the entirety of the [CII] in the Eastern tail, $\Sigma_{SFR} = 4 \times 10^{-5} M_{\odot} \text{ yr}^{-1} \text{ kpc}^{-2}$. This value is 4 times larger than the value from $\Sigma_{SFR}(H\alpha)$, but still 8 times less than the expected value from the gas density. However, Boselli et al. (2002) find that the dispersion in their SFR correlation ~ 10 . So a factor of 4 difference is within the scatter. They do say that [CII] line luminosity can be taken as a star formation indicator for normal late-type galaxies ($8.0 < \log L_{FIR} < 10.5$), but may be not applicable to ULIRGs. The NGC 2782 galaxy itself is a LIRG with an IRAS luminosity of $1.6 \times 10^{44} \text{ erg s}^{-1}$ which is at the high end of this range. However, we study the tidal tails which would have lower FIR emission than the central regions of the merger. Whether to use [CII] as a direct indicator for star formation is a matter of some debate, however, there have been recent calibrations of the SFR from [CII] for different regimes such as starbursts (De Looze et al. 2011) and HII regions in M33 (Mookerjea et al. 2011).

The global $\Sigma_{SFR}(H\alpha)$ calculated for these tidal tails is two to three orders of magnitude lower than those found in spiral galaxies as well as dwarf galaxies. Kennicutt (1998) find that $-3.3 < \log(\Sigma_{SFR}) < -0.8$ in 61 normal spiral galaxies. The Milky Way galaxy has $\Sigma_{SFR} = 3.6 \times 10^{-3} M_{\odot} \text{ yr}^{-1} \text{ kpc}^{-2}$ (Naab & Ostriker 2006). The LMC has a global star formation rate of $0.4 M_{\odot} \text{ yr}^{-1}$ which gives $\Sigma_{SFR} = 1.5 \times 10^{-3} M_{\odot} \text{ yr}^{-1} \text{ kpc}^{-2}$. The SMC has a global star formation rate of $0.05 M_{\odot} \text{ yr}^{-1}$ which gives $\Sigma_{SFR} = 1.9 \times 10^{-4} M_{\odot} \text{ yr}^{-1} \text{ kpc}^{-2}$ (Wilke et al. 2004).

The $\Sigma_{SFR}(gas)$ is similar in magnitude to values in the LMC and SMC. The Magellanic Stream is a very nearby example of a gas tail of presumably tidal origin that has no star formation associated with it. Putman et al. (2003) measured the total HI gas mass in the Stream to be $2.1 \times 10^8 M_{\odot}$. Converting the angular size of the Stream ($100^{\circ} \times 10^{\circ}$) using a distance of 55 kpc (Putman et al. 2003), we infer a size of the Magellanic Stream to be 940.9 kpc^2 . Using the resulting gas density of $\Sigma_{HI} = 2.2 \times 10^5 M_{\odot} \text{ kpc}^{-2}$, the Magellanic Stream

has an expected $\Sigma_{SFR} = 3 \times 10^{-5} \text{ M}_{\odot}\text{yr}^{-1} \text{ kpc}^{-2}$ which is two orders of magnitude lower than that calculated for the Western tidal tail of NGC 2782 and four orders of magnitude lower than the Eastern tail.

The difference between the Σ_{SFR} values calculated from the $\text{H}\alpha$ flux and that predicted from the gas density may indicate a lower star formation efficiency (Knierman et al. 2012). However, the $\text{H}\alpha$ SFR is a lower limit since it only traces massive star formation in the last 5 Myr. Also, the $\text{H}\alpha$ emission may depend on the masses of the star clusters formed. If the tails only formed lower mass star clusters where few high mass stars reside, similar to the Taurus-Auriga region (Kenyon, Gomez, & Whitney 2008), there would be young, blue star clusters but a lack of widespread $\text{H}\alpha$ emission. The Western tail has only one small in size HII region, but several other blue star cluster candidates. *Galaxy Evolution Explorer (GALEX)* All-sky Imaging Survey (AIS; Morrissey et al. 2007) images show faint UV emission along the Western tail, indicating a young stellar population, probably dominated by B and A stars (Knierman et al. 2012; Torres-Flores et al. 2012). In addition, the emission is concentrated only in specific areas in both tails rather than being spread over the tail region. This may indicate that global star formation rates from $\text{H}\alpha$ or [CII] are not an accurate assessment of the total star formation in the tails.

4.3.2. Star Formation on Local Scales

We also examine the star formation on local scales in both tails using $\text{H}\alpha$ and [CII]. Table 9 shows the SFR from $\text{H}\alpha$ for these massive HI clumps using Kennicutt (1998) which range from 0.0016-0.008 $\text{M}_{\odot}\text{yr}^{-1}$ in the Eastern tail and 0.015 $\text{M}_{\odot}\text{yr}^{-1}$ for the Western tail source. The Western tail source has a factor of 2-3 higher SFR than TDGC and E-HI-S the two most luminous $\text{H}\alpha$ sources in the Eastern tail. Using the [CII] luminosity and the equation for SFR from Boselli et al. (2002), the range of SFR in the Eastern tail is 0.017-0.035 $\text{M}_{\odot}\text{yr}^{-1}$ and $< 0.02 \text{ M}_{\odot}\text{yr}^{-1}$ in the Western tail. The SFR is a factor of 7 larger from [CII] than from $\text{H}\alpha$ for E-HI-S the most luminous [CII] source in the Eastern tail while for TDGC, $\text{SFR}([\text{CII}]) = 4 \text{ SFR}(\text{H}\alpha)$. We expect a lower $\text{SFR}(\text{H}\alpha)$ than $\text{SFR}([\text{CII}])$ since $\text{H}\alpha$ is affected by extinction and also only traces the most recent star formation. That the $\text{SFR}([\text{CII}])$ is larger than $\text{H}\alpha$ may indicate that star formation in the Eastern tail may proceed differently due to its origin as a "splash region". However, in the Western tail the HII source has $\text{SFR}(\text{H}\alpha)$ similar to the upper limit for the $\text{SFR}([\text{CII}])$. Since the Eastern tail shows a higher $\text{SFR}([\text{CII}])$ than $\text{SFR}(\text{H}\alpha)$, the at most equal values in the Western tail, but likely lower $\text{SFR}([\text{CII}])$ indicates that perhaps something is happening in the Western tail to suppress [CII] emission.

These comparisons may be affected by differing areas, so we calculate the SFR per area (Σ_{SFR}) to compare regions. The local values for SFR per area from $H\alpha$ are $2 - 11 \times 10^{-4} M_{\odot} \text{yr}^{-1} \text{kpc}^{-2}$ for the regions in the Eastern tail. The TDGC region has a similar Σ_{SFR} to the Western tail $H\alpha$ region ($\Sigma_{SFR} = 1 \times 10^{-3} M_{\odot} \text{yr}^{-1} \text{kpc}^{-2}$). The remainder of the Eastern tail sources are 2-4 times lower than the Western tail source. This seems to indicate local star formation as indicated by $H\alpha$ is occurring at similar levels in each tail. The $\Sigma_{SFR}([CII])$ in the Eastern tail ranges from $2.5 - 4.5 \times 10^{-3} M_{\odot} \text{yr}^{-1} \text{kpc}^{-2}$ and in the Western Tail is $< 1.1 \times 10^{-3} M_{\odot} \text{yr}^{-1} \text{kpc}^{-2}$. The TDGC region has the highest $\Sigma_{SFR}([CII])$ at 2 times the other two detected regions and this region is 4 times larger than the limit in the Western tail.

Using the total gas surface density, we find even higher expected star formation rates. In the Eastern tail, we expect Σ_{SFR} of 0.05-0.18 $M_{\odot} \text{yr}^{-1} \text{kpc}^{-2}$. Due to the non-detection of CO in the Western tail, the star formation rates from the gas density are upper limits. Even so, these upper limits are lower than the Eastern tail by a factor of 10-40 ($\Sigma_{SFR}(gas) < 0.005 - 0.009 M_{\odot} \text{yr}^{-1} \text{kpc}^{-2}$).

In summary, on local scales, we find the Western tail HII region has the highest SFR using $H\alpha$ as a tracer, but has a low SFR using its upper limit in $[CII]$. This indicates that $[CII]$ is suppressed relative to $H\alpha$ in the Western tail. The Eastern tail has a higher SFR from $[CII]$ as compared to $H\alpha$ perhaps indicating that this "splash region" has a different star formation law than in normal galaxies. Normalized to area, we find similar SFR per unit area in both tails using $H\alpha$ as a tracer. This seems to indicate that star formation is occurring locally at similar rates in both tails. The expected SFR per area from the local gas density is higher than that observed by both $H\alpha$ and $[CII]$ indicating that there may be a lower SFE at the local level in both tails as well. Comparing the tails, the expected local SFR surface density from the observed local gas density is 14-40 times higher in the Eastern tail than in the Western tail. This indicates that there is a larger gas reservoir for star formation in the Eastern tail at least on local scales.

4.4. Star Formation Efficiency

Having calculated the SFR for each region, we now examine the star formation efficiency (SFE) for these local regions. Boquien et al. (2011) use multiwavelength data of major merger Arp 158 to study the local Schmidt-Kennicutt law. They find that star forming regions in the tidal debris follow a different Schmidt-Kennicutt law than those in the central regions of the merger, falling along a line of similar slope to Daddi et al. (2010), but offset so that the same gas density gives lower values of SFR. As discussed in Knierman et al.

(2012), W235 is consistent with the other star forming regions in the tidal debris of Arp 158 indicating a lower SFE than in the central region of Arp 158. If we compare the Eastern tail star forming regions to the tidal debris of Arp 158, we find that for their given total gas surface density, their star formation rates from $H\alpha$ lie more than 2 dex below the relation for the tidal debris of Arp 158 indicating a substantially lower SFE in the Eastern tail.

We calculate the gas depletion timescales (τ_{dep}) or the amount of time it would take for the current SFR to deplete the gas (either molecular or atomic). The SFE is the inverse of the gas depletion time. Table 11 lists region, depletion timescale of molecular gas mass vs. SFR from $H\alpha$ ($\tau_{dep,H_2} = M_{mol}/SFR_{H\alpha}$), depletion timescale of neutral gas mass vs. SFR from $H\alpha$ ($\tau_{dep,H I} = M_{HI}/SFR_{H\alpha}$), depletion timescale of molecular gas mass vs. SFR from [CII] ($\tau_{dep,H_2} = M_{mol}/SFR_{[CII]}$), and depletion timescale of neutral gas mass vs. SFR from [CII] ($\tau_{dep,H I} = M_{HI}/SFR_{[CII]}$) for the local and global regions in both tails.

The highest SFE ($\tau_{dep,H_2} < 1.5$ Gyr) is in the Western tail HII region considering the molecular gas limit and $H\alpha$ SFR. This is comparable to the molecular gas depletion timescales determined for the star forming regions in Arp 158 ($\tau_{dep} \sim 0.5 - 2$ Gyr; Boquien et al. 2011) and in TDGs ($\tau_{dep} \sim 0.8 - 4$ Gyr; Braine et al. 2001). These ranges are also similar to the average gas depletion timescales in spiral galaxies. If we use the value for the CO emission assumed in the discussion of Torres-Flores et al. (2012) using an analog HII region in the tidal debris near NGC 3077, we might expect it to have molecular mass of $1.5 \times 10^6 M_{\odot}$. If we use this value for the molecular mass, $\tau_{dep,H_2} = 0.1$ Gyr, making this region similar to gas depletion timescales in dwarf galaxies (1 -100 Myr). If this molecular mass is close to the actual value, this would mean that this region is highly efficient at making stars.

Considering neutral gas and SFR from $H\alpha$, TDGC and W235 ($\tau_{dep,H I} = 5 - 7.7$ Gyr) are less efficient than normal star forming regions. But these areas are still more efficient at star formation than outer regions of spiral galaxies at r_{25} ($\tau_{dep,H I} \sim 20$ Gyr) or dwarf galaxies at r_{25} ($\tau_{dep,H I} \sim 40$ Gyr). Using the molecular gas and $H\alpha$ SFR, TDGC and E-HI-S have depletion timescales of 33 Gyr and 38 Gyr similar to these less efficient regions. Bigiel et al. (2010) find very low SFE ($\tau_{dep,H I} \sim 100$ Gyr) in the outer disks of spiral galaxies using FUV and HI observations. Even less efficient than outer disk regions is the E-HI-mid region. Smith et al. (1999) also found low star formation efficiency in the Eastern tail using the ratio of $L_{H\alpha}/M_{H_2}$. Overall, our results comparing SFR($H\alpha$) and gas mass indicate that on local scales the Western tail is more efficient at forming stars than the Eastern tail.

Considering molecular gas and SFR from [CII], the Western tail limit remains with the highest SFE, however, both the gas mass and SFR([CII]) are upper limits. In the Eastern tail, E-HI-S has the highest SFE, but with a depletion timescale of 5.6 Gyr is still less efficient

than normal star forming galaxies. Considering the neutral gas, TDGC has the highest SFE ($\tau_{\text{dep,H I}} = 1.3$) indicating efficient star formation. Using [CII], the Western tail is also more efficient at star formation than most of the Eastern tail except for TDGC considering its H I mass.

Since the CO observations were taken with a large beam, we examine the Eastern tail on larger scales. Even if we consider the total molecular and neutral hydrogen for the entire Eastern tail, the SFE remains low (16-43 Gyr). For the Western tail as a whole, we sum the limits from the three CO pointings and use the total H I mass from Smith (1994). The Western tail has a low SFE considering the molecular gas mass limits and the single H II region (< 12 Gyr), but is very inefficient considering the H I mass of the tail (133 Gyr). So on global scales, it appears that the Western tail is less efficient at forming stars.

On both global and local scales, it appears the Western tail is more efficient at forming stars than the Eastern tail. The Western tail also lacks high mass star clusters and star cluster complexes which are hosted in the Eastern tail. These two points are not inconsistent. In the Eastern tail, star cluster complexes of higher mass will form many more high mass stars than isolated lower mass star clusters in the Western tail. These high mass stars provide feedback and energy into the ISM in the form of stellar winds and supernova. This feedback can suppress further star formation and have a lower SFE in the area. In addition, Smith et al. (1999) suggest that the Eastern tail formed as a “splash” region (versus a tidal region of merger debris) and may have inhibited star formation due to gas heating during the encounter. A tidally formed region such as the Western tail, would have gravitational compression and possibly enhanced star formation. Given the higher SFE in the Western tail, this may be evidence for gravitational compression in the tidal tail.

5. Conclusions

Tidal tails provide laboratories for star formation under extreme conditions very different from quiescent galaxy disks. With low gas pressures and densities and smaller amounts of stable molecular gas they are perhaps on the edge of the parameter space open to star formation.

The two tails of NGC 2782 are an interesting place to consider in this discussion. The Western tail is rich in H I gas, but CO is not observed in the massive H I knots in the tail, leading Braine et al. (2001) to conclude that H I “...has presumably not had time to condense into H₂ and for star formation to begin.” This study finds that at least 10 star clusters have formed in the Western tail based on the overdensity of bright, blue objects in the tail. The

Western tail also hosts a bright HII region which was explored in Knierman et al. (2012) while 6 additional young regions are found in FUV and NUV by Torres-Flores et al. (2012) and in H α by Werk et al. (2011). Clearly the lack of *observable* CO does not guarantee the absence of recent star formation. It may play a role, however, in the properties of star clusters forming therein since the Western tail lacks high mass star clusters and star cluster complexes. The Eastern tail has a dense knot of HI and CO-rich gas at its base. Based on the overdensity calculations, at least 14 young star clusters are observed in this region of the tail. The Eastern tail also hosts several HII regions (Smith et al. 1999), of which we discover [CII] associated with five of these regions. In contrast, the Western tail H α source shows only an upper limit on [CII] contrary to expectations based on its bright HII region and its HI column density.

We examined in turn the reasons for the differences between the two tails: ambient pressure, gas phase, SFR, amount of gas available for star formation, and efficiency of star formation.

Ambient pressure: Based on the calculation for M_{char} in local regions in the Western tail, we find that the M_{char} in the Eastern tail is only slightly larger than in the Western tail. We surmise that the relatively small difference between the predicted clump mass in the two tails indicates that the ambient pressure between the two tails is not very different. However, there is a large difference between M_{char} and the upper limit on molecular mass in the Western tail indicating that the Western tail is deficient in molecular mass (or at least, in CO).

Gas phase: We find that the Western tail has much less molecular gas mass (traced by CO) for its neutral hydrogen mass than the Eastern tail. This indicates that CO may be suppressed in the Western tail. Both tails are lower in their [CII] intensity based on their HI as compared to observations of nearby galaxies and Galactic regions. The Eastern tail HI regions are close, but still below, the expected [CII] values for “standard” HI clouds while the Western tail limit is a few times below that. We also find a lower $I_{[CII]}/I_{CO}$ in the Eastern tail than studies of nearby star forming galaxies and Galactic HII regions which is in line with GMCs and normal galaxies.

SFR: Using the entire tail area, we find that the global SFR from H α and from [CII] are much less than the SFR expected from the gas surface density suggesting that both tails have low SFE. On local scales, we find the Western tail HII region has the highest SFR from H α , but has only an upper limit for SFR from [CII]. This indicates that [CII] emission is suppressed in the Western tail relative to H α . Normalized to their areas, we find similar local $\Sigma_{SFR}(H\alpha)$ in both tails indicating that star formation is occurring similarly on the local scale in both tails. For each local region, the expected SFR from the gas density is

higher than from $H\alpha$ or $[CII]$ indicating lower SFE at the local level as well. Comparing the two tails, the expected local SFR density from the gas density in the Eastern tail is 14-40 times higher than in the Western tail.

Gas Reservoirs for SF: We examined different tracers for the reservoirs of gas for star formation in these two tidal tails and found that these tracers were not consistent. Both tails have abundant neutral hydrogen gas, but the Eastern tail has more molecular gas (traced by CO) and ionized gas (traced by $[CII]$). However, the Western tail has a higher local SFR and both tails have similar SFR per unit area, indicating that star formation according to $H\alpha$ emission is similar in both tails. If we use $[CII]$ emission as a SFR tracer, we find that the Eastern tail has a higher SFR than the Western tail. Looking at gas density, the Eastern tail has a higher total gas surface density than the Western tail. So we expect a higher SFR per area in the Eastern tail. That these tracers are not consistent between the tails indicates that something different is going on between the tails. In the Western tail, the non-detections in CO and $[CII]$ compared to its HI and $H\alpha$ may be due to its inability to produce detectable CO or $[CII]$ emission. This may be due to a deficiency in carbon even though it has a high oxygen abundance, because the tail material is going through its first generation of stars and has not had enough time to build up a higher carbon abundance.

SFE: By calculating the gas depletion timescales for molecular gas and neutral hydrogen, we examine SFE in the tails. As discussed in Knierman et al. (2012), the Western tail HII region has a normal SFE when considering its molecular mass upper limit, but less efficient star formation if we consider its neutral hydrogen mass. The Eastern tail regions have a low SFE, in some cases as low as spiral or dwarf galaxies at r_{25} . We suggest that the lower SFE in the Eastern tail may be due to its more massive star clusters providing feedback to prevent further star formation. Also, the Eastern tail may have a lower SFE due to its formation mechanism as a splash region where gas heating has a higher effect. The Western tail has a higher SFE even though it has a lower local gas surface density than the Eastern tail, possibly due to its tidal formation where gravitational compression has more of an effect and can increase star formation.

We acknowledge helpful discussions with J. Lee, S. Malhotra, P. Young, J. Monkiewicz, and J. Funes. We wish to thank R. Kennicutt for use of his $H\alpha$ filter. We thank the anonymous referee for very helpful suggestions which have improved this paper. KK acknowledges support by the University of Arizona/NASA Space Grant Graduate Fellowship (2004-2006) and also by NASA through an award issued by JPL/Caltech. ISK is the recipient of a John Stocker Postdoctoral Fellowship from the Science and Industry Research Fund. We used the NASA/IPAC Extragalactic Database (NED) which is operated by JPL, California Institute of Technology, under NASA contract. We acknowledge the usage of the HyperLeda database

(<http://leda.univ-lyon1.fr>). This work is based on observations with the *Vatican Advanced Technology Telescope (VATT)*: the Alice P. Lennon Telescope and the Thomas J. Bannan Astrophysics Facility, with Herschel, a European Space Agency Cornerstone Mission with significant participation by NASA, and with the Kitt Peak 12 Meter which is operated by the Arizona Radio Observatory (ARO), Steward Observatory, University of Arizona.

Table 11. Comparison of Star Formation Efficiencies Between Eastern and Western Tails

Location	$\tau_{\text{dep,H2,H}\alpha}$ (Gyr)	$\tau_{\text{dep,H1,H}\alpha}$ (Gyr)	$\tau_{\text{dep,H2,[CII]}}$ (Gyr)	$\tau_{\text{dep,H1,[CII]}}$ (Gyr)
East				
TDGC	33	5	8.2	1.3
H I-N	81	160	>70	>141
H I-M	232	200	21	18
H I-S	38	81	5.6	12
E Tail	16 ^a	43	2.7 ^a	7
West				
H I-N	<29 ^a	>240		
H I-M	<1.5	7.7	<1.4 ^b	>7.3
H I-S	<53 ^b	>390		
W Tail	< 12	133	< 4 ^b	> 45

^aUsing observations from this work.

^bBoth gas mass and SFR are upper limits.

REFERENCES

- Adelman-McCarthy, J. K., et al. 2008, *ApJS*, 175, 297
- Arnett, D. 1996, *Supernovae and Nucleosynthesis*, Princeton University Press, Princeton
- Bastian, N. et al. 2005 *A&A*, 433, 79
- Bastian, N. et al. 2005, *A&A*, 435, 65.
- Bigiel, F., Leroy, A., Walter, F., Blitz, L., Brinks, E., de Blok, W.J.G., & Madore, B. 2010, *AJ*, 140, 1194
- Bik, A., Lamers, H.J.G.L.M, Bastian, N., Panagia, N., & Romaniello, M. 2003, *A&A*, 397, 473
- Blitz, L. & Rosolowsky, E. 2006, *ApJ*, 650, 933.
- Boquien, M., Lisenfeld, U., Duc, P.-A., Braine, J., Bournaud, F., Brinks, E., & Charmandaris, V. 2011, *A&A*, 533, 19
- Boselli, A., Gavazzi, G., Lequeux, J. & Pierini, D. 2002, *A&A*, 385, 454
- Bournaud, F., Duc, P.-A., Amram, P., Combes, F., Gach, J.-L. 2004, *A&A*, 425, 813
- Braine, J., et al. 2001, *A&A*, 378, 51
- Bresolin, F. & Kennicutt, R.C. 1997, *AJ*, 113, 975
- Bruzual, G., & Charlot, S. 2003, *MNRAS*, 344, 1000
- Daddi, E., Elbaz, D., Walter, F., et al. 2010, *ApJL*, 714, 118
- De Looze, I., Baes, M., Bendo, G., Cortese, L., & Fritze, J. 2011, *MNRAS*, 416, 2712
- Devereux, N. A. 1989, *ApJ*, 346, 126
- Dolphin, A. 2009, *PASP*, 121, 655
- Duc, P.-A., Bournaud, F., & Masset, F. 2004, *A&A*, 427, 803
- Elmegreen, B.G. & Hunter, D.A. 2004, *AJ*, 128, 2170
- Elmegreen, B. G., Kaufman, M., & Thomasson, M. 1993, *ApJ*, 412, 90
- Elmegreen, D.E., & Salzer, J.J. 1999, *AJ*, 117, 764

- Ferreiro, D. L., Pastoriza, M. G. & Ricketts, M. C. 2008, 481, 645
- Genzel, R., Tacconi, L.J., Combes, F., et al. 2012, ApJ, 746, 69
- Grogin, N.A., Lucas, R.A., Golimowski, D., & Biretta, J. 2010, HST WFPC2 Instrument Science Report, 3, 1
- Holmberg, E. 1958, Lund Obs. Medd. II, 136, 1
- Hibbard, J. E., Guhathakurta, P., van Gorkom, J. H., & Schweizer, F. 1994, AJ, 107, 67
- Hollenbach, D.J., & Tielens, A.G.G.M. 1997, ARA&A, 35, 179
- Jester, S., Schneider, D. P., Richards, G., Green, R., Schmidt, M., et al. 2005, AJ, 130, 873
- Kennicutt, R.C. 1998, ARA&A, 36, 189
- Kenyon, S. J., Gomez, M., & Whitney, B. A. 2008, Handbook of Star Forming Regions, Volume I, ed. B. Reipurth, 405
- Knierman, K. A., Hunsberger, S. D., Gallagher, S. C., Charlton, J. C., Whitmore, B. C., Kundu, A., Hibbard, J. E., & Zaritsky, D. 2003, AJ, 126, 1227
- Knierman, K. A., Knezek, P. M., Scowen, P., Jansen, R., & Wehner, E. 2012, ApJ, 749, L1
- Konstantopoulos, I.S., Gallagher, S.C., Fedotov, K., Durrell, P.R., Heiderman, A., Elmegreen, D.M. et al. 2010, ApJ, 723, 197
- Konstantopoulos, I.S., Gallagher, S.C., Fedotov, K., Durrell, P.R., Tzanavaris, P., Hill, A.R., et al. 2012, ApJ, 745, 30
- Lee, J. 2006, Ph.D. Thesis, University of Arizona
- Leroy, A.K., Bolatto, A., Gordon, K., et al. 2011, ApJ, 737, 12
- Mathis, J. S. 1990, ARA&A, 28, 37
- Maybath, A., Masiero, J., Hibbard, J. E., Charlton, J. C., Palma, C., Knierman, K., & English, J. 2007, MNRAS, 381, 59
- Mihos, C.J., Bothun, G.D., & Richstone, D.O. 1993, ApJ, 418, 82
- Mookerjee, B. et al. 2011, A&A, 232, 152
- Morrissey, P., Conrow, T., Barlow, T., et al. 2007, ApJS, 173, 682

- Mould, J. R., Huchra, J.P., Freedman, W. L., Kennicutt, R.C., Ferrarese, L., Ford, H.C., et al. 2000, *ApJ*, 529, 786
- Mullan, B., Konstantopoulos, I.S., Kepley, A.A., et al. 2011, *ApJ*, 731, 93
- Oberst, T.E., Parshely, S.C., Stacey, G.J., Nikola, T. et al. 2006 *ApJL*, 652, L125
- Naab, T. & Ostriker, J. 2006, *MNRAS*, 366, 899
- Oke, J. B. 1990, *AJ*, 99, 1621
- Paturel G., Petit C., Prugniel P., Theureau G., Rousseau J., Brouty M., Dubois P., Cambrésy L., 2003, *A&A*, 412, 45
- Pilbratt, G.L., Riedinger, J.R., Passvogel, T. et al. 2010, *A&A*, 518, L1
- Poglitsch, A., Waelkens, C., Geis, N. et al. 2010, *A&A*, 518, L2
- Portegies Zwart, S., McMillan, S. & Gieles, M. 2010, *ARA&A*, 48,431
- Putman, M. E., Staveley-Smith, L., Freeman, K. C., Gibson, B. K., Barnes, D. G. 2003, *ApJ*, 586, 170
- Robin, A. C., Reyl, C., Derrire, S., & Picaud, S. 2003, *A&A*, 409, 523
- Rosolowsky, E., Keto, E., Matsushita, S., Willner, S. P. 2007, *ApJ*, 661, 830
- Schlaafy, E.F., & Finkbeiner, D.P. 2011, *ApJ*, 737, 103
- Schlegel, D.J., Finkbeiner, D.P., & Davis, M. 1998, *ApJ*, 500, 525
- Schombert, J. M., Wallin, J. F., & Struck–Marcell, C. 1990, *AJ*, 99, 497
- Smith, B. 1994, *AJ*, 107, 1695
- Smith, B. et al. 1999, *AJ*, 117, 1237
- Stacey, G. et al. 1991, *ApJ*, 373, 423
- Torres-Flores, S., et al. 2012, *MNRAS*, 421, 3612
- Trancho, G., Bastian, N., Schweizer, F., Miller, B. W. 2007, *ApJ*, 658, 993
- van Zee, L., et al. 1998, *AJ*, 116, 2805

- Vandenbussche, B., Blommaert, J., Contursi, A., et al. 2011, PACS Spectroscopy Performance & Calibration, 2.4, 1
- Walter, F., Martin, C. L., & Ott, J. 2006, AJ, 132, 2289
- Wehner, E. 2005, Ph.D. Thesis, University of Wisconsin - Madison.
- Weilbacher, P. M., Fritze-v.Alvensleben, U., Duc, P.-A., & Fricke, K. J. 2002, ApJ, 579, L79
- Werk, J. K., Putman, M.E., Meurer, G., R., Santiago-Figueroa, N. 2011, ApJ, 735, 71
- Whitmore, B., Zhang, Q., Leitherer, C., Fall, S.M., Schweizer, F., & Miller, B. 1999, AJ, 118, 1551
- Wilke, K. et al. 2004, A&A, 414, 69
- Wolfire, M., Hollenbach, D., & McKee, C. F., 2010, ApJ, 716, 1191
- Yoshida, M., Taniguchi, Y., & Murayama, T. 1994, PASJ, 46, 195L